

## Pore solution composition of alkali-activated slag/fly ash pastes

Zuo, Yibing; Nedeljkovic, Marija; Ye, Guang

**DOI**

[10.1016/j.cemconres.2018.10.010](https://doi.org/10.1016/j.cemconres.2018.10.010)

**Publication date**

2019

**Document Version**

Accepted author manuscript

**Published in**

Cement and Concrete Research

**Citation (APA)**

Zuo, Y., Nedeljkovic, M., & Ye, G. (2019). Pore solution composition of alkali-activated slag/fly ash pastes. *Cement and Concrete Research*, 115, 230-250. <https://doi.org/10.1016/j.cemconres.2018.10.010>

**Important note**

To cite this publication, please use the final published version (if applicable). Please check the document version above.

**Copyright**

Other than for strictly personal use, it is not permitted to download, forward or distribute the text or part of it, without the consent of the author(s) and/or copyright holder(s), unless the work is under an open content license such as Creative Commons.

**Takedown policy**

Please contact us and provide details if you believe this document breaches copyrights. We will remove access to the work immediately and investigate your claim.

# 1 Pore solution composition of alkali-activated slag/fly ash pastes

2

3 Yibing Zuo, Marija Nedeljković, Guang Ye

4

5 Section of Materials and Environment, Faculty of Civil Engineering and Geosciences, Delft University of  
6 Technology, Stevinweg 1, 2628 CN Delft, The Netherlands

7

8 **Abstract:** The pore solutions of a series of hardened alkali-activated slag/fly ash pastes were  
9 extracted by the steel-die method, and analyzed using ICP-OES analysis technique. According to  
10 the saturation index from thermodynamic calculations, the pore solutions of alkali-activated slag  
11 pastes kept oversaturated with respect to solid reaction products with time. In the pore solutions  
12 of alkali-activated fly ash pastes, an increase of temperature (from 40 °C to 60 °C) led to  
13 decreases of the concentrations of Si, Al, Ca, Na, OH<sup>-</sup>, K, Fe and Mg, while the soluble silicate in  
14 the alkaline activator resulted in increases of the concentrations of these elements. Compared to  
15 the alkali-activated slag paste with the same alkaline activator, 50% replacement of slag by fly  
16 ash did not result in a substantial change of the pore solution composition. Based on the  
17 experimental results, conceptual models were proposed to describe the elemental concentrations  
18 in the pore solutions.

19

20 **Keywords:** alkali activation; slag/fly ash; pore solution; saturation index; conceptual models

21

22

23

24

## 25 **1 Introduction**

26  
27 Alkali-activated materials (AAMs) are a class of materials obtained by the chemical reaction of a  
28 powdered aluminosilicate precursor (most commonly blast furnace slag and/or fly ash) with an  
29 alkaline activator (usually a solution of sodium hydroxide and/or sodium silicate) at ambient or  
30 elevated temperature [1, 2]. Due to the ability to utilize high-volume of industrial by-products as  
31 the powdered aluminosilicate precursors, AAMs can save a large amount of fossil fuel-derived  
32 energy. As such, 80% or greater reduction of CO<sub>2</sub> emission can be achieved by AAMs when  
33 compared to ordinary Portland cement (OPC) based materials [3, 4]. Besides, AAMs release  
34 lower amount of heat [5], and provide comparable or even superior mechanical properties and  
35 durability performance [3, 6-9]. Therefore, AAMs show very promising potential for utilization  
36 to embrace a sustainable future global construction materials industry [2].

37  
38 Pore solution is an essential component of AAMs. It is in this medium where the powdered  
39 aluminosilicate precursors dissolve and subsequently a set of reactions take place to produce solid  
40 reaction products. The role of pore solution can be viewed in the following three aspects.

- 41
- 42 • *Dissolution kinetics.* The high concentration of OH<sup>-</sup> ions in the pore solution allow  
43 breaking of bonds such as Si-O and Al-O on the surface of aluminosilicate precursors [10].  
44 A higher alkalinity of pore solution will accelerate the dissolution kinetics [11-15].  
45 Therefore, from the kinetics point of view, pore solution composition determines the  
46 dissolution kinetics of aluminosilicate precursors. The dissolution kinetics determines the  
47 degree of reaction and thus controls the reaction kinetics and the amount of solid reaction  
48 products produced with time.

49

50 • *Thermodynamics.* Thermodynamics is of great significance to the understanding of  
51 chemical reactions [16]. The reactions of AAMs, same as any other chemical system,  
52 follow the law of thermodynamics. When aluminosilicate precursors are brought into  
53 contact with an alkaline activator, their constituents start to dissolve and subsequently  
54 various solid reaction products start to be formed if the solution is saturated or  
55 oversaturated with respective the solids. At the given temperature and pressure, the pore  
56 solution composition controls the ongoing reaction process and determines what reaction  
57 products are to be formed [17, 18].

58

59 • *Durability.* The dominant phase assemblage in AAMs is an alkali calcium-aluminosilicate  
60 hydrate (C-(N-)A-S-H) type gel or a three-dimensional hydrous alkali-aluminosilicate (N-  
61 A-S-H) type gel, depending on the Ca content in the system [1]. From the durability point  
62 of view, the high alkalinity of pore solution ensures the stability of calcium-  
63 aluminosilicate hydrates [19] and alkali-aluminosilicate gels [20] in AAMs. If AAMs are  
64 embedded with reinforcing steel, the pore solution plays a more important role by forming  
65 a passive film on the surface of steel rebars and, consequently, avoiding corrosion of steel  
66 rebar [21, 22].

67

68 Those three aspects illustrate the significance of pore solution in AAMs. Furthermore, the  
69 chemical properties (chemical composition, and amorphous content etc.) and physical properties  
70 (surface morphology, and particle size etc.) of aluminosilicate precursors vary significantly from  
71 different sources [1, 5, 23]. For this reason, the alkali activation of aluminosilicate precursors  
72 greatly relies on the pore solution. However, studies regarding the pore solution composition in

73 AAMs are few for alkali-activated slag paste [12, 24-26], and even rarely reported for alkali-  
74 activated fly ash paste and alkali-activated slag blended with fly ash paste.

75  
76 Song and Jennings studied the pore solution chemistry of alkali-activated slag and found that  
77 higher alkalinity of pore solution led to higher concentrations of Si and Al and lower  
78 concentrations of Ca and Mg [24]. In another study regarding the relationship between the  
79 composition of pore solution and the composition and structure of the main reaction products in  
80 alkali-activated slag paste, the researchers found that the nature of the alkaline activator  
81 influenced the structure and composition of the produced calcium silicate hydrate [25]. In  
82 comparison with the pore solution of OPC-based materials, the pore solution of alkali-activated  
83 slag paste showed ten times lower concentration of Ca and tens to hundreds of times higher  
84 concentrations of Si and Na [12]. It was reported that the initiation of pitting at the steel-cement  
85 concrete interface started only after the concentration ratio of  $\text{Cl}^-$  relative to  $\text{OH}^-$  exceeded a  
86 particular value [22]. This suggests a great dependence of passivation of reinforcing steel on the  
87 alkalinity of the pore solution. Because of little soluble Ca available in the pore solution of alkali-  
88 activated slag to play a buffering role similar to  $\text{Ca}(\text{OH})_2$  in OPC-based materials, the alkalinity  
89 of pore solution of alkali-activated slag is mainly maintained by the content of alkali [26].  
90 Therefore, it is essential to provide sufficient amount of alkalis to ensure protection of reinforcing  
91 steel from corrosion.

92  
93 In this study, the pore solutions of alkali-activated slag, alkali-activated fly ash and alkali-  
94 activated slag blended with fly ash pastes were studied by means of the inductively coupled  
95 plasma-optical emission spectroscopy (ICP-OES) analysis technique. The influences of alkaline  
96 activator and temperature on the pore solution composition were investigated. The measured

97 composition of the pore solution and its changes with time can be used to predict the (potentially)  
98 solid reaction products. Thus, the pore solutions of alkali-activated slag pastes were  
99 thermodynamically analyzed in terms of effective saturation index. In the meantime, solid phase  
100 analysis was conducted through the X-ray diffraction (XRD) and Fourier transform infrared  
101 spectroscopy (FTIR). Based on the experimental results, conceptual models were proposed to  
102 describe the elemental concentrations in the pore solutions. The obtained results will contribute to  
103 new insights regarding the chemistry of pore solution and thermodynamic modelling in AAMs.

104

## 105 **2 Materials and methods**

106

### 107 **2.1 Materials and mixtures**

108

109 In this study, ground granulated blast furnace slag and fly ash were used as the aluminosilicate  
110 precursors to prepare alkali-activated slag/fly ash pastes. The chemical compositions of blast  
111 furnace slag and fly ash were determined by X-ray fluorescence spectrometry (XRF), and are  
112 listed in Table 1. The X-ray diffraction patterns of slag and fly ash are plotted in Figure 1. Quartz,  
113 mullite and hematite were the three crystalline phases identified in fly ash. In order to determine  
114 the amorphous content of fly ash, corundum ( $\alpha\text{-Al}_2\text{O}_3$ ) was added as an internal standard to  
115 replace 20% of fly ash. Through the Rietveld analysis method [27], the amorphous content of fly  
116 ash was determined as 71%. By subtracting  $\text{SiO}_2$  and  $\text{Al}_2\text{O}_3$  in the crystalline phases from the  
117 total  $\text{SiO}_2$  and  $\text{Al}_2\text{O}_3$ , the reactive  $\text{SiO}_2$  and  $\text{Al}_2\text{O}_3$  were determined as 37% and 15% respectively.  
118 These results agree with the measurements by a previous colleague using the chemical  
119 dissolution treatment (we used a similar fly ash from the same manufacture plant in Netherlands)  
120 [28]. For slag, no crystalline phase was identified from the X-ray diffraction pattern. This is

121 consistent with the fact that the ground granulated blast furnace slag usually contains more than  
122 95% vitreous phase [29].

123

124 **Table 1** Chemical compositions of blast furnace slag and fly ash (by weight, %)

125

126 **Figure 1** X-ray diffraction patterns of slag and fly ash. In the graph, Q, M and H refer to quartz, mullite and hematite  
127 respectively.

128

129 Sodium hydroxide (analytical grade, >98%) and water glass (8.25 wt.% Na<sub>2</sub>O, 27.5 wt.% SiO<sub>2</sub>  
130 and 64.25 wt.% H<sub>2</sub>O) were used to prepare two types of alkaline activators: sodium hydroxide  
131 activator and sodium silicate activator. As shown in Table 2, a series of alkaline activators with  
132 different contents of Na<sub>2</sub>O and SiO<sub>2</sub> were used to prepare alkali-activated slag pastes, alkali-  
133 activated fly ash pastes and alkali-activated slag blended with fly ash pastes. In the notations for  
134 the samples, N and S indicate weight percentage of Na<sub>2</sub>O and SiO<sub>2</sub> with respect to the precursor,  
135 T indicates temperature in Celsius and B indicates blend of slag and fly ash. The Na<sub>2</sub>O in alkaline  
136 activator consists of the Na<sub>2</sub>O from sodium hydroxide and the Na<sub>2</sub>O from water glass. For alkali-  
137 activated slag pastes and alkali-activated slag blended with fly ash pastes, water to precursor ratio  
138 was 0.4. For alkali-activated fly ash pastes, water to precursor ratio was 0.35. Here, the water in  
139 water glass was also included in the calculation of the water to precursor ratio of the pastes.  
140 According to the type of alkaline activator, the samples were categorized into two systems:  
141 sodium hydroxide activated system (with no soluble silicate in the alkaline activator) and sodium  
142 silicate activated system (with soluble silicate in the alkaline activator).

143

144 **Table 2** Mixture compositions and curing temperature

145

146 According to the materials characterization described previously, fly ash contains glassy  
147 (amorphous) and crystalline constituents in nature, e.g. quartz, mullite and hematite. Compared to  
148 slag, fly ash has much lower reactivity. Therefore, elevated temperature curing is usually applied  
149 for the alkali activation of fly ash in order to obtain a relatively high strength at early ages [28,  
150 30]. The elevated temperature leads to an acceleration of the dissolution of fly ash and the  
151 polymerization process of alkali-aluminosilicate type gel [1, 31]. In this study, two elevated  
152 temperatures (40 °C and 60 °C) were used to investigate the influence of temperature on the pore  
153 solution composition. For all samples, sealed curing was applied until testing.

154  
155 The pH and concentrations of Na, Si, and OH<sup>-</sup> in the alkaline activators are listed in Table 3.  
156 These results were obtained through the thermodynamic calculations using a thermodynamic  
157 software. This software is introduced in the section 2.3. In sodium hydroxide solution, aqueous  
158 sodium hydroxide (NaOH(aq)) normally exists. For this reason, the measured concentration of  
159 OH<sup>-</sup> through titration against hydrochloride acid includes the hydroxide from NaOH(aq). The  
160 details of titration against hydroxide acid are given in section 2.2. As derived by thermodynamic  
161 calculations, two values of the concentration of OH<sup>-</sup>, e.g. including and excluding hydroxide from  
162 NaOH(aq), are provided in Table 3. A big difference can be seen between those two values for  
163 each alkaline activator, and the concentration of OH<sup>-</sup> including hydroxide from NaOH(aq) is  
164 closer to that in the pore solution of alkali-activated slag/fly ash pastes, as obtained by titration.

165  
166 **Table 3** The pH and concentrations of Na, Si, and OH<sup>-</sup> in the alkaline activators

167

168 2.2 Pore solution analysis via ICP-OES

169

170 The pore solutions of hardened samples were extracted using the steel-die method as described  
171 by Barneyback and Diamond [32]. Pressures of up to 300 MPa were used to extract the pore fluid  
172 from the samples at different curing ages. After extraction, the pore solution was immediately  
173 filtered using Whatman 41 filter paper. One part of the filtered solution was diluted using nitric  
174 acid (0.2 vol.%). The diluted solutions were analyzed through a PerkinElmer Optima 5300DV  
175 ICP-OES spectrometer, by which the concentrations of Si, Al, Ca, Na, K, Fe and Mg were  
176 determined.

177  
178 The concentration of  $\text{OH}^-$  was measured by titration against hydrochloride acid (0.1 mol/L).  
179 Phenolphthalein was used as the indicator. First, a volume ( $V_1$ , ml) of pore solution was  
180 accurately measured using a pipette and injected into a beaker. Then a drop of phenolphthalein  
181 was added into the beaker, and the solution turned red. Afterwards, hydrochloride acid was  
182 slowly added into the beaker through a burette until the solution turned colorless. While adding  
183 hydrochloride acid, the beaker was swirled with hand. After the titration, the amount of  
184 hydrochloride acid added into the beaker was measured as  $V_2$  (ml). Then the concentration of  
185  $\text{OH}^-$  ( $[\text{OH}^-]$ , mol/L) could be determined as:

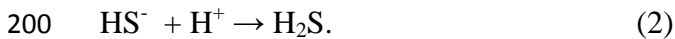
186  
187 
$$[\text{OH}^-] = 0.1 * V_2 / V_1 \quad (1)$$

188  
189 In the titration test, two replicates of each pore solution were titrated, and the average  $[\text{OH}^-]$  was  
190 presented as the final result.

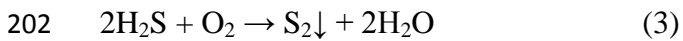
191  
192 For the measurement of S, another part of the filtered solution was diluted using sodium  
193 hydroxide solution (0.1 mol/L) instead of nitric acid, and subsequently subject to ICP-OES

194 analysis. This is because S mostly exists as sulfide ( $\text{HS}^-$ ) in the pore solution [12, 33]. The  
195 dilution with nitric acid will acidify  $\text{HS}^-$  and lead to formation of  $\text{H}_2\text{S}$  as described by Equation  
196 (2). On one hand,  $\text{H}_2\text{S}$  evaporates and results in a characteristic foul odor of rotten eggs, as  
197 experienced during the dilution process using nitric acid. On the other hand,  $\text{H}_2\text{S}$  may be oxidized  
198 and lead to white precipitation of sulfur as described by Equation (3), and shown in Figure 2.

199



201



203

204 Figure 2 shows the white precipitation under the scanning electron microscope (SEM) and its  
205 element composition using energy dispersive spectroscopy. This finding confirmed the fact that  
206 acid dilution resulted in white precipitation of sulfur. For this reason, the measured  
207 concentrations of S using nitric acid dilution for alkali-activated slag paste were not correct and  
208 thus not presented in this study.

209

210 **Figure 2** White precipitation and its element composition in diluted pore solution using nitric acid.

211

### 212 2.3 Thermodynamic analysis of pore solution

213

214 Thermodynamics is essential to the understanding of chemical reactions. Whether a solid can  
215 potentially form or not can be predicted through the saturation index (SI) [17].

216

$$217 \quad \text{SI} = \log(\text{IAP}/\text{K}_{\text{S}0}) \quad (4)$$

218  
219 where IAP and  $K_{S0}$  are the ion activity product and equilibrium solubility product of a solid  
220 respectively. A positive SI indicates oversaturation and thus the possibility that this solid phase  
221 can precipitate. If SI is negative, it means under-saturation and implies that this solid is unstable  
222 in equilibrium within such a solution. A SI of zero indicates equilibrium between solution and  
223 solid. However, SI can be misleading when comparing phases which dissociate into a different  
224 number of ions (N) [17]. For this reason, effective saturation index (ESI) is applied in this study  
225 for thermodynamic analysis of pore solution.

226

$$227 \quad \text{ESI} = \text{SI}/N \quad (5)$$

228

229 Before performing the thermodynamic analysis of the pore solution, it is crucial to obtain the  
230 thermodynamic database. In AAMs, the thermodynamic database is only available for alkali-  
231 activated slag. For alkali-activated fly ash, the thermodynamic data have not been established yet.  
232 For this reason, the thermodynamic analysis was only performed for the pore solutions of the  
233 alkali-activated slag pastes. The Gibbs energy minimization software GEM-Selektor v.3  
234 (<http://gems.web.psi.ch/>) [34, 35] and the thermodynamic database developed in [36, 37] for  
235 alkali-activated slag were used. The activities of ions were calculated using the measured  
236 elemental concentrations as the input.

237

#### 238 2.4 Measurement of heat evolution rate

239

240 The heat evolution rate was measured using an isothermal calorimeter by following standard  
241 ASTM C1679 [38]. For the measurements of heat evolution at the elevated temperatures (40 °C

242 and 60 °C), internal mixing was used to avoid any temperature difference. Fly ash and alkaline  
243 activator were conditioned in the calorimeter at the measurement temperature. When the thermal  
244 equilibrium was reached, the alkaline activator was injected into the glass ampoule to be mixed  
245 with aluminosilicate precursor powder internally. Subsequently, the heat release rate was  
246 recorded.

247

248 2.5 X-ray diffraction (XRD) and Fourier transform infrared spectroscopy (FTIR)

249

250 XRD analysis was performed on the powdered samples using a Philips X'Pert diffractometer  
251 applying  $\text{CuK}_\alpha$  radiation ( $\lambda = 1.54 \text{ \AA}$ ). The samples were scanned between  $5^\circ$  and  $70^\circ$  2-theta,  
252 with a step size of  $0.02^\circ$  2-theta and a dwell time of 5 s per step. FTIR was performed using a  
253 Spectrum TM 100 Optical ATR-FTIR spectrometer over the wavelength range of 600 to 4000  
254  $\text{cm}^{-1}$  with a resolution of  $4 \text{ cm}^{-1}$ .

255

### 256 **3 Results and discussion**

257

#### 258 3.1 Pore solution composition of alkali-activated slag paste

259

260 Figure 3 presents the concentrations of Si, Al, Ca, OH, K and Na (hereafter denoted as [Si], [Al],  
261 [Ca], [OH], [K] and [Na] respectively) in the pore solution of alkali-activated slag paste as a  
262 function of time up to 28 days. The pore solution data are listed in the Appendix. The pore  
263 solution composition was dominated by Na and OH<sup>-</sup>, whereas much lower concentrations of Si,  
264 Al, K and Ca were observed. The most significant changes in the compositions of pore solutions  
265 in alkali-activated slag pastes took place during the first hours up to 3 days. This can be seen

266 from the changes of elemental concentrations with time, particularly the decreases of the [Si],  
267 [Na] and [OH<sup>-</sup>]. The concentrations of Si, Al and Ca were in the order: [Si] > [Al] > [Ca]. The  
268 developments of the elemental concentrations with time will be further discussed in the section  
269 3.5.

270  
271 **Figure 3** Elemental concentrations in the pore solutions of alkali-activated slag pastes. In the graphs, N and S  
272 indicate weight percentage of Na<sub>2</sub>O and SiO<sub>2</sub> with respect to slag. The water to slag ratio was 0.4 and the curing  
273 temperature was 20 °C.

274  
275 There was a strong decrease of [Si] during the initial period up to 3 days, and then the decrease of  
276 [Si] continued gradually with time for all samples. For sodium hydroxide activated slag system,  
277 the [Si] increased with the increase of Na<sub>2</sub>O content. For sodium silicate activated system, the  
278 [Si] increased with the increase of Na<sub>2</sub>O content after 1 day. The [Si] in the pore solution of  
279 sodium silicate activated slag paste was much higher than that in the sodium hydroxide activated  
280 slag paste with the same content of Na<sub>2</sub>O. The higher [Si] for sodium silicate activated slag paste  
281 was a result of the soluble Si in the sodium silicate activator. For all the alkali-activated slag  
282 samples, the [Al] decreased slightly with time. The increase of Na<sub>2</sub>O content in alkaline activator  
283 led to an obvious increase of the [Al].

284  
285 The [OH<sup>-</sup>] decreased over time and increased with the increase of Na<sub>2</sub>O content. Comparing the  
286 sodium silicate activated sample to the sodium hydroxide activated sample with the same content  
287 of Na<sub>2</sub>O, it can be seen that the added SiO<sub>2</sub> from alkaline activator resulted in a decrease of [OH<sup>-</sup>]  
288 ]. The [OH<sup>-</sup>] indicates a pH in the range of 13.77~14.67 up to 28 days in the pore solution. This  
289 shows a higher alkalinity than that in the pore solution (pH>12) buffered by Ca(OH)<sub>2</sub> in OPC-

290 based materials, and much higher than the pH of 9.5 below which corrosion commences [39].  
291 The [Ca] remained at a very low level (0.2~2 mmol/L) and did not show much change over time.

292  
293 An apparent decrease of [Na] was observed during the first 3 days in Figure 3(E). And then the  
294 [Na] decreased slightly with progressive reaction of slag. When the Na<sub>2</sub>O content increased from  
295 4% to 8%, the [Na] increased for both the sodium hydroxide activated slag system and the  
296 sodium silicate activated slag system. On the contrary to the [Na], the [K] increased with time.  
297 This was because K was sourced from slag and increased with the dissolution of slag, while Na  
298 was mainly sourced from the alkaline activator and decreased as it was taken up into the calcium  
299 aluminosilicate hydrates [33, 40, 41].

300  
301 In the pore solution of alkali-activated slag, the concentrations of Mg and Fe were not presented  
302 since they were below the detection limit of ICP-OES. The detection limit of Mg and Fe are  
303 0.0042 mmol/L and 0.0009 mmol/L respectively. The concentration of Mg below the detection  
304 limit was attributed to the formation of a hydrotalcite-like phase in alkali-activated slag as seen  
305 from the XRD patterns (see Figure 8). The formation of hydrotalcite led Mg within the pore  
306 solution into hydrotalcite, and thus resulted into low concentration of Mg. The concentration of  
307 Fe below the detection limit was because of the low content of Fe<sub>2</sub>O<sub>3</sub> in slag (0.46%). On the  
308 contrary, the concentrations of Mg and Fe were obtained for the alkali-activated fly ash pastes,  
309 which will be presented in section 3.3. This was because of no Mg containing phase detected in  
310 alkali-activated fly ash (see Figure 11) and much higher content of Fe<sub>2</sub>O<sub>3</sub> in fly ash (6.6%).

311  
312 The plots of the concentrations of Na, Al and Ca as a function of the concentration of OH<sup>-</sup> are  
313 shown in Figure 4(A). In pore solutions, the positive charge of Na is mostly balanced by the

314 negative hydroxide ion. Higher [Na] leads to higher [OH<sup>-</sup>]. For this reason, the concentration of  
315 Na increased linearly with the increase of the concentration of OH<sup>-</sup> and this relationship was  
316 independent of the type of alkaline activator. In pore solutions, the concentration of Ca remained  
317 at a very low level and slightly decreased as the concentration of OH<sup>-</sup> increased. This could be  
318 attributed to the common ion effect [42, 43]. The pore solutions had high concentrations of Si,  
319 OH<sup>-</sup> and Na<sup>+</sup>. Those ions might combine with Ca to form solid reaction products (see Table 4)  
320 and thus lowered the Ca concentration in the pore solution. This point could be further supported  
321 by thermodynamic analysis of pore solution (see section 3.2). The ESI with respect to C-(N-)A-  
322 S-H and secondary reaction products were mostly larger than zero, which indicates oversaturation  
323 and likely precipitation of these solid phases in pore solution. Therefore, Ca stayed on a low  
324 concentration and the increase of [OH<sup>-</sup>] led to a decrease of the [Ca] in the pore solution.

325  
326 The [Al] increased with the increase of [OH<sup>-</sup>] in the pore solution for both the sodium hydroxide  
327 activated slag system and the sodium silicate activated slag system, which is consistent with the  
328 finding in the literature [24]. However, this relationship only exists for the samples using the  
329 same type of alkaline activator. Using the alkaline activator with the same content of Na<sub>2</sub>O, the  
330 sodium hydroxide activated slag paste (e.g. N4S0) had higher [OH<sup>-</sup>] in the pore solution than that  
331 of the sodium silicate activated slag paste (e.g. N4S5.4). But the pore solution of sodium  
332 hydroxide activated slag paste (e.g. N4S0) had a lower [Al] than that of sodium silicate activated  
333 slag paste (e.g. N4S5.4). This was because of the different calcium aluminosilicate hydrates  
334 formed as a consequence of the different types of alkaline activators used in the alkali activation  
335 of slag. The calcium aluminosilicate hydrate formed in the sodium hydroxide activated slag paste  
336 had a higher structural order than that formed in the sodium silicate activated slag paste [25]. This  
337 is also found in this work by XRD analysis (see Figure 8). For sodium hydroxide activated

338 samples (for instance N4S0), the peak that corresponded to C-(N-)A-S-H, was sharper and had a  
339 higher intensity than that for sodium silicate activated slag samples (for instance N4S5.4).  
340 Furthermore, C-S-H(I) was detected in sodium hydroxide activated slag samples while it was not  
341 in sodium silicate activated slag samples. As such, the calcium aluminosilicate hydrate formed in  
342 sodium hydroxide activated slag had higher structural order and degree of crosslinking. The  
343 higher structural order and degree of crosslinking of calcium aluminosilicate hydrate stabilized its  
344 structure, which could lead to a lower solubility. The lower solubility of calcium aluminosilicate  
345 hydrate resulted in lower solubility of Al and thus lower [Al] in the pore solution of sodium  
346 hydroxide activated slag paste.

347  
348 **Figure 4** Concentrations of one element as a function of the concentration of another element in pore solution. (A):  
349 [Na], [Al] and [Ca] versus [OH<sup>-</sup>]. (B): [Si] versus [OH<sup>-</sup>]. (C) [Si] versus [Ca]. In the graphs, N and S indicate the  
350 weight percentage of Na<sub>2</sub>O and SiO<sub>2</sub> with respect to slag. The curing temperature was 20 °C. The water to slag ratio  
351 was 0.4.

352  
353 In alkaline solutions, the solubility of Si increases with the increase of the alkalinity of solution  
354 [11]. This is also observed in the pore solution of sodium hydroxide activated slag paste [24]. In  
355 this study, the relationship between the alkalinity of pore solution and the solubility of Si was  
356 more comprehensively studied for sodium hydroxide activated slag pastes and sodium silicate  
357 activated slag pastes. Figure 4(B) shows the plots between the concentration of Si and the  
358 concentration of OH<sup>-</sup> in the pore solution. The [Si] increased with the increase of [OH<sup>-</sup>] in the  
359 pore solution for each alkali-activated slag paste. The plots suggest the existence of two separate  
360 lines as shown in Figure 4(B). The line with a higher [Si] is associated with the sodium silicate  
361 activated slag pastes, while the line with a lower [Si] corresponds to the sodium hydroxide

362 activated slag pastes. From the sodium hydroxide activated slag system to the sodium silicate  
363 activated slag system, the concentration of Si moves up and backward as indicated by the arrows.  
364 This is because of the addition of SiO<sub>2</sub> from the sodium silicate activator. On one hand, the  
365 addition of SiO<sub>2</sub> resulted in higher [Si] in the pore solution and thus an up translation of the plot.  
366 On the other hand, the addition of SiO<sub>2</sub> resulted in lower alkalinity of pore solution, e.g. lower  
367 [OH], and thus a backward translation of the plot.

368  
369 Figure 4(C) plots the concentration of Si as a function of the concentration of Ca. As marked with  
370 a dashed black line in the graph, a decreasing trend was generally observed between the  
371 concentrations of Si and Ca, which is in line with the literature [24, 44]. The fact that the  
372 concentration of Si decreased with the increasing concentration of Ca was attributed to the  
373 common ion effect. Excess of Ca within pore solution could combine Si into solid reaction  
374 products and thus result in a lower concentration of Si.

375  
376 3.2 Thermodynamic analysis of the pore solution of alkali-activated slag paste

377  
378 As it is directly encoded in GEM-Selektor, the extended Debye-Huckel equation is used to  
379 calculate the ion activity coefficients [34, 35]. The extended Debye-Huckel equation is accurate  
380 at moderate ionic strengths (up to ~1-2 molal) [45]. Figure 5 presents the ionic strengths in the  
381 pore solution of alkali-activated slag paste. The ionic strengths in the pore solutions of N4S0,  
382 N4S5.4 and N6S5.4 were within 1-2 molal. In the pore solutions of N6S0, N8S0 and N8S5.4, the  
383 ionic strengths were larger than 2 molal, beyond the valid range (~1-2 molal). However, use of an  
384 improved aqueous phases model, such as the Pitzer model [46], is limited in the current version  
385 of GEM-Selektor. This is because the description of aqueous silicate species in the database of

386 GEM-Selektor does not extend beyond dimeric silicate and aluminosilicate units [36]. On the  
387 other hand, GEM-Selektor has been commonly used in the thermodynamic modelling of the  
388 hydration of alkali-activated slag (with ionic strengths ~1-3 molal in the pore solution [12]), and  
389 the modelling results agreed well with the experimental data [37, 47, 48]. As such, slight excess  
390 of ionic strengths (> 2 molal) would not impose a serious impact on the calculation results. Since  
391 the measured elemental concentrations, including the concentration of OH<sup>-</sup>, were used as input to  
392 calculate the activities of aqueous ions with GEM-Selektor, the calculated pH agreed with the  
393 measured one.

394  
395 **Figure 5** The ionic strengths in the pore solutions of alkali-activated slag pastes, calculated by GEM-Selektor. In the  
396 graphs, N and S indicate the weight percentage of Na<sub>2</sub>O and SiO<sub>2</sub> with respect to slag. The curing temperature was  
397 20 °C. The water to slag ratio was 0.4.

398  
399 Myers et al. used a set of eight CNASH<sub>ss</sub> end-members to describe the calcium aluminosilicate  
400 hydrates in alkali-activated slag [36]. These eight end-members and their corresponding  
401 dissociation reactions and equilibrium solubility products are presented in Table 4. Among the  
402 eight end-members for the calcium aluminosilicate hydrates, 5CA and INFCa are two C-A-S-H  
403 gel end-members, 5CNA and INFCNA are two C-N-A-S-H gel end-members, INFCN is a C-N-  
404 S-H gel end-member, and T2C\*, T5C\* and TobH\* are three C-S-H gel end-members. The  
405 equilibrium solubility products of these eight end-members were used to calculate the effective  
406 saturation indexes as described in section 2.3.

407  
408 **Table 4** Chemical reactions and equilibrium solubility products at 25°C and 1 bar for eight end-members and  
409 crystalline reaction products in alkali-activated slag

410  
411 Figure 6 presents the effective saturation indexes with respect to the eight end-members. For the  
412 sodium hydroxide activated slag pastes (the left column in Figure 6), the pore solutions were  
413 oversaturated with respect to 5CA, 5CNA, INFCNA, INFCN, T2C\* and T5C. The effective  
414 saturation indexes with respect to those end-member gels decreased with time during the initial  
415 period (up to 3 days). This indicates the continuous formation of the calcium aluminosilicate  
416 hydrates. The formation of the calcium aluminosilicate hydrates reduced the degree of  
417 oversaturation and thus led to decreases of the effective saturation indexes. After the initial  
418 period, the reaction of slag slowed down and stepped into a steady reaction stage controlled by  
419 diffusion processes [49]. In this reaction stage, there might exist a dynamic equilibrium between  
420 the dissolution of slag and the formation of the calcium aluminosilicate hydrates. For this reason,  
421 the effective saturation indexes with respect to 5CA, 5CNA, INFCNA, INFCN, T2C\* and T5C  
422 showed no substantial change with time. Although the increase of Na<sub>2</sub>O content resulted in  
423 higher alkalinity of the pore solution, it did not lead to significant influence on the effective  
424 saturation indexes with respect to the eight end-members.

425  
426 For sodium silicate activated slag pastes (the right column in Figure 6), similar results were  
427 found. Compared to those for the sodium hydroxide activated slag pastes, the effective saturation  
428 indexes with respect to the eight end-members were slightly higher for the sodium silicate  
429 activated slag pastes. The slightly higher effective saturation indexes were attributed to the larger  
430 activity coefficients of SiO<sub>3</sub><sup>2-</sup> and Ca<sup>2+</sup> (two valence electrons) than those of Na<sup>+</sup> and OH<sup>-</sup> (one  
431 valence electron). It can be seen in Figure 6 that the pore solution of sodium silicate activated  
432 slag paste had higher concentrations of Si, Al and Ca than that of sodium hydroxide activated

433 slag paste. As such, the pore solution of sodium silicate activated slag paste had higher effective  
434 saturation indexes with respect to the eight end-members.

435  
436 **Figure 6** Effective saturation indexes with respect to the eight end-members as functions of time. In the graphs, N  
437 and S indicate the weight percentage of  $\text{Na}_2\text{O}$  and  $\text{SiO}_2$  with respect to slag. The curing temperature was  $20^\circ\text{C}$ . The  
438 water to slag ratio was 0.4. A ESI of 0 indicates equilibrium between solution and solid; a positive ESI indicates  
439 oversaturation and a negative ESI indicates undersaturation.

440  
441 In addition to the calcium aluminosilicate hydrates, some crystalline reaction products are also  
442 identified in alkali-activated slag, such as hydrotalcite [50], tetracalcium aluminate hydrate  
443 ( $\text{C}_4\text{AH}_{13}$ ) [50], katoite ( $\text{C}_3\text{AH}_6$ ) [37] and stratlingite ( $\text{C}_2\text{ASH}_8$ ) [51]. The dissociation reactions  
444 and equilibrium solubility products of  $\text{C}_2\text{ASH}_8$ ,  $\text{C}_3\text{AH}_6$ ,  $\text{C}_4\text{AH}_{13}$  and portlandite ( $\text{Ca}(\text{OH})_2$ ) are  
445 listed in Table 4. These products were also captured according to the effective saturation index  
446 from thermodynamic calculations. Figure 7 plots the effective saturation indexes with respect to  
447  $\text{C}_2\text{ASH}_8$ ,  $\text{C}_3\text{AH}_6$ ,  $\text{C}_4\text{AH}_{13}$  and  $\text{Ca}(\text{OH})_2$  for the sodium hydroxide activated slag pastes (left  
448 column) and the sodium silicate activated slag pastes (right column). Since the concentration of  
449 Mg was not measured, the effective saturation index with respect to hydrotalcite was not  
450 calculated. The effective saturation indexes with respect to  $\text{C}_2\text{ASH}_8$ ,  $\text{C}_3\text{AH}_6$ ,  $\text{C}_4\text{AH}_{13}$  and  
451  $\text{Ca}(\text{OH})_2$  increased rapidly during the initial period. This is in the contrast to the effective  
452 saturation indexes with respect to 5CA, 5CNA, INFCNA, INFCN, T2C\* and T5C. It indicates  
453 that the calcium aluminosilicate hydrate is thermodynamically favored to form at early age, while  
454 the crystalline reaction products are thermodynamically favored to form at a later age. After the  
455 initial period, the effective saturation indexes with respect to these four crystalline phases showed  
456 no substantial change with time. The effective saturation indexes with respect to these four



481 **Figure 8** X-ray diffraction patterns of N4S0, N8S0 and N4S5.4 at 28 days. In the graphs, N and S indicate the weight  
482 percentage of Na<sub>2</sub>O and SiO<sub>2</sub> with respect to slag. The curing temperature was 20 °C. The water to slag ratio was 0.4.

483

484 3.3 Pore solution composition of alkali-activated fly ash paste

485

486 Figure 9 presents the measured concentrations of Si, Al, OH<sup>-</sup>, Ca, Na, K, Fe, Mg and S in the  
487 pore solution of alkali-activated fly ash pastes as a function of time up to 28 days (672 hours).

488 The pore solution data are listed in the Appendix. The pore solution composition was dominated  
489 by Na, OH<sup>-</sup> and Si, whereas much lower concentrations of Al, K, Ca, Fe and Mg were observed.

490 The most significant changes in the compositions of pore solutions in alkali-activated fly ash  
491 pastes took place during the first week. This can be seen from the changes of elemental

492 concentrations with time, particularly the decreases of the [Si], [Na] and [OH<sup>-</sup>]. The  
493 concentrations of Si, Al and Ca were in the order: [Si] > [Al] > [Ca]. The developments of the

494 elemental concentrations with time will be further discussed in the section 3.5. The increase of  
495 curing temperature from 40 °C to 60 °C led to decreases of the concentrations of Si, Al, OH<sup>-</sup>, Ca,

496 Na, K, Fe and Mg. The influence of temperature on the pore solution composition of alkali-  
497 activated fly ash paste will be discussed in the section 3.6.

498

499 **Figure 9** Elemental concentrations in the pore solutions of alkali-activated fly ash pastes where N and S indicate the  
500 weight percentage of Na<sub>2</sub>O and SiO<sub>2</sub> with respect to fly ash, and T indicates the curing temperature in Celsius. The  
501 water to fly ash ratio was 0.35.

502

503 It can be seen from Figure 9(A) that the [Si] decreased with time for all alkali-activated fly ash  
504 pastes. As the Na<sub>2</sub>O content increased from 6.2% to 9.3%, the [Si] increased for both curing

505 temperatures. The [Si] was much higher in the sodium silicate activated fly ash paste than that in  
506 the sodium hydroxide activated fly ash paste with the same content of Na<sub>2</sub>O. This was attributed  
507 to the soluble silica added from the alkaline activator prepared using sodium silicate solution.

508  
509 As shown in Figure 9(B), the [Al] decreased with time for all alkali-activated fly ash samples.  
510 For the sodium hydroxide activated fly ash pastes, the [Al] increased slightly as the Na<sub>2</sub>O content  
511 increased from 6.2% to 9.3%. When the sodium silicate was added in the alkaline activator, the  
512 [Al] increased significantly in comparison with the sodium hydroxide activated fly ash with the  
513 same content of Na<sub>2</sub>O, e.g. N9.3S9T40 in comparison with N9.3S0T40, and N9.3S9T60 in  
514 comparison with N9.3S0T60. The significantly increased [Al] in the sodium silicate activated fly  
515 ash paste was due to the enhanced dissolution of fly ash by the soluble silicate.

516  
517 In the sodium hydroxide activated fly ash paste, the initial preferential dissolution of Al from the  
518 fly ash created a siliceous layer on the fly ash grains [57-59]. The initially dissolved aqueous Al  
519 species then might absorb to the surface sites on the siliceous layer, passivating the surface by  
520 preventing the approach of hydroxide ions [60]. Thus, the dissolution of fly ash **could be** slowed  
521 down. In the sodium silicate activated fly ash paste, the soluble silicate could quickly complex  
522 the initial preferentially released Al. This prevented Al from absorbing to the surface sites and  
523 thus reduced the surface passivation and allowed more rapid dissolution of fly ash [61]. It was  
524 reported that the soluble silicate enhanced greater structural breakdown of the frameworks in fly  
525 ash if the concentration of Si in the alkaline activator was larger than 213.6 mmol/L [61]. In this  
526 study, the concentration of Si in the alkaline activator for the sodium silicate activated fly ash  
527 pastes (Table 3) was 4170 mmol/L, twenty times larger than 213.6 mmol/L. As a result, the  
528 dissolution of Si, Al, Ca, K, Fe and Mg from fly ash was enhanced.

529

530 The enhanced dissolution of fly ash by soluble silicate can be also supported by the calorimetry  
531 data. Figure 10 presents the heat evolution rates of sodium hydroxide activated fly ash and  
532 sodium silicate activated fly ash cured at 40 °C and 60 °C. Two calorimetric peaks could be  
533 identified on the heat evolution rate curves of sodium hydroxide activated fly ash samples cured  
534 at 40 °C and 60 °C. The first calorimetric peak ( $P_1$ ) corresponds to the dissolution/wetting of fly  
535 ash, and the second calorimetric peak ( $P_2$ ) corresponds to the acceleration of polymerization  
536 process of alkali-aluminosilicate type gel [62]. Compared to sodium hydroxide activated fly ash  
537 samples, only one peak was identified on the heat evolution rate curves of sodium silicate  
538 activated fly ash samples cured at 40 °C and 60 °C. The calorimetry data clearly illustrate the  
539 effect of soluble silicate on the dissolution of fly ash. In the sodium hydroxide activated fly ash,  
540 the absorbed Al passivated the surface of fly ash and slowed down the dissolution of fly ash. As a  
541 result, the acceleration of polymerization of alkali-aluminosilicate type gel was delayed and thus  
542 led to the occurrence of the second calorimetric peak. In the sodium silicate activated fly ash, the  
543 soluble silicate reduced the surface passivation and allowed rapid dissolution of fly ash.  
544 Consequently, the polymerization of alkali-aluminosilicate type gel was accelerated. As such, the  
545 calorimetric peak that corresponded to the polymerization was advanced and thus merged into the  
546 calorimetric peak that corresponded to the dissolution/wetting of fly ash. For this reason, the  
547 second calorimetric peak was not readily identified.

548

549 **Figure 10** Heat evolution rates of sodium hydroxide activated fly ash and sodium silicate activated fly ash cured at  
550 40 °C and 60 °C: (A) N9.3S0T40 in comparison with N9.3S9T40; and (B) N9.3S0T60 in comparison with  
551 N9.3S9T60. In the graphs,  $P_1$  and  $P_2$  refer to the first and second calorimetric peak respectively, N and S indicate the

552 weight percentage of  $\text{Na}_2\text{O}$  and  $\text{SiO}_2$  with respect to fly ash, and T indicates the curing temperature in Celsius. The  
553 water to fly ash ratio was 0.35.

554  
555 From Figure 9(C), it is clear that the  $[\text{OH}^-]$  decreased with time, and increased significantly with  
556 increase of  $\text{Na}_2\text{O}$  content for both curing temperatures. When sodium silicate was used as the  
557 alkaline activator, the  $[\text{OH}^-]$  decreased significantly in comparison with the sodium hydroxide  
558 activated fly ash with the same content of  $\text{Na}_2\text{O}$ . The decreased alkalinity caused by the increased  
559 modulus of alkaline activator ( $\text{SiO}_2/\text{Na}_2\text{O}$ ) is in agreement with [63]. The  $[\text{OH}^-]$  indicates a pH  
560 range of 13.08~14.07 up to 28 days of curing. This pH range shows a higher alkalinity in the pore  
561 solution of alkali-activated fly ash than that in the pore solution ( $\text{pH}>12$ ) buffered by  $\text{Ca}(\text{OH})_2$  in  
562 OPC based materials, and is much higher than the pH of 9.5 below which steel reinforcement  
563 corrosion commences [39].

564  
565 The concentration of Ca is plotted in Figure 9(D). The pore solution of sodium silicate activated  
566 fly ash paste had higher  $[\text{Ca}]$  than that of sodium hydroxide activated fly ash paste with the same  
567 content of  $\text{Na}_2\text{O}$ . This can be attributed to the lower alkalinity of pore solution and the enhanced  
568 dissolution of fly ash by the soluble silicate. The  $[\text{Ca}]$  decreased with time, which is different  
569 from the  $[\text{Ca}]$  in the pore solutions of alkali-activated slag pastes where no substantial change of  
570 the  $[\text{Ca}]$  was observed. The decrease of  $[\text{Ca}]$  was due to the precipitation of Ca into solid reaction  
571 products, which was also observed in [61]. The precipitation of Ca into solid reaction products  
572 was further evidenced by the solid phase analysis through XRD. Figure 11 presents the XRD  
573 patterns of alkali-activated fly ash samples at 28 days. It can be seen that new crystalline phases  
574 were formed in addition to quartz (Q), mullite (M) and hematite (H). Chabazite (C) was formed  
575 in sodium hydroxide activated fly ash samples, while faujasite (F) was formed in sodium silicate

576 activated fly ash samples. Both of chabazite and faujasite contain Ca. In addition to the Ca  
577 containing crystalline phases, Ca might be also incorporated into N-A-S-H gels [64]. It has been  
578 reported that Na may be displaced by Ca through ion exchange on the surface of N-A-S-H,  
579 resulting in N-(C-)A-S-H gels [65].

580  
581 **Figure 11** X-ray diffraction patterns of alkali-activated fly ash samples cured at 40 °C and 60 °C: (A) N9.3S0T40  
582 and N9.3S0T60; and (B) N9.3S9T40 and N9.3S9T60. In the graphs, Q, M, H, C, F and A refer to quartz, mullite,  
583 hematite, chabazite, faujasite and analcime respectively, N and S indicate the weight percentage of Na<sub>2</sub>O and SiO<sub>2</sub>  
584 with respect to fly ash, and T indicates the curing temperature in Celsius. For all samples, the water to fly ash ratio  
585 was 0.35.

586  
587 Figure 9(E) showed an apparent decrease of [Na] with time. When the Na<sub>2</sub>O content increased  
588 from 6.2% to 9.3%, the [Na] increased in the sodium hydroxide activated fly ash system. From  
589 Figure 9(F), it is clear that the [K] decreased as a function of time for all samples, which is on the  
590 contrary to the [K] in the pore solutions of alkali-activated slag pastes (Figure 3(F)). In the  
591 sodium hydroxide/silicate activated fly ash based materials, sodium based crystalline phases are  
592 normally identified, such as Na-chabazite and hydroxysodalite [66, 67]. On the contrary,  
593 potassium based crystalline phases are rarely reported. This is due to the better zeolitization  
594 capabilities of sodium cations than those of potassium cations since the sodium cations are  
595 smaller than the potassium cations [68]. So, the decrease of [K] was most likely to be attributed  
596 to the formation of potassium-aluminosilicate (K-A-S-H) type gels. The formation of K-A-S-H in  
597 alkali-activated fly ash has been reported in the literature [69, 70]. The increase of Na<sub>2</sub>O content  
598 from 6.2% to 9.3% did not show much influence on [K]. Comparing the sodium silicate activated  
599 fly ash paste to the sodium hydroxide activated fly ash paste with the same content of Na<sub>2</sub>O, the

600 [K] increased about two times. This could be due to the enhanced dissolution of fly ash by the  
601 soluble silicate.

602  
603 The concentrations of Fe and Mg in the pore solutions of alkali-activated fly ash pastes are  
604 plotted as a function of time in Figure 9(G) and Figure 9(H) respectively (hereafter denoted as  
605 [Fe] and [Mg] respectively). It is clear that the concentrations of Fe and Mg decreased with time.  
606 Since the dissolution of fly ash is enhanced in the sodium silicate activated fly ash paste, the  
607 concentrations of Fe and Mg were higher when compared to those in the sodium hydroxide  
608 activated fly ash paste with the same content of Na<sub>2</sub>O.

609  
610 Figure 9(I) plots the concentration of S as a function of time (hereafter denoted as [S]). The [S]  
611 increased with time for all alkali-activated fly ash samples. For sodium hydroxide activated fly  
612 ash, the [S] increased with increase of Na<sub>2</sub>O content. Fly ash contains 0.73% of SO<sub>3</sub> (see Table  
613 1). If the S in the fly ash is completely dissolved in the alkaline activator, the concentration of S  
614 is around 250 mmol/L. However, the [S] measured in the pore solution was around 350 mmol/L,  
615 much larger than 250 mmol/L. This was because of the decrease of the solution volume resulted  
616 from the dissolution/wetting of fly ash and the polymerization process of alkali-aluminosilicate  
617 type gel. It is known that the porosity of alkali-activated fly ash decreases with time [28]. This  
618 indicates the decrease of the volume of solution in the alkali-activated fly ash. Therefore, using  
619 the volume of alkaline activator to calculate the concentration of S would result in  
620 underestimation.

621  
622 3.4 Pore solution composition of alkali-activated slag blended with fly ash paste

623

624 To study the influence of the replacement of slag by fly ash on the pore solution composition, one  
625 mixture of alkali-activated slag blended with fly ash was used in this study. Figure 12(A) presents  
626 the elemental concentrations in the pore solution of alkali-activated slag blended with fly ash  
627 (N6S5.4B). The pore solution data are listed in the Appendix. It can be seen that [Si], [Na] and  
628 [OH<sup>-</sup>] decreased as a function of time, while [Al] and [Ca] did not show much change with time.  
629 The [OH<sup>-</sup>] indicates a pH range of 14.05~14.37 up to 28 days. Compared to the alkali-activated  
630 slag (N6S5.4) with the same contents of Na<sub>2</sub>O and SiO<sub>2</sub> as shown in Figure 12(B), 50 wt.%  
631 replacement of slag by fly ash did not result in a substantial change on the pore solution  
632 composition of alkali-activated slag blended with fly ash paste.

633  
634 **Figure 12** Elemental concentrations in the pore solutions of alkali-activated slag blended with fly ash paste (A), and  
635 alkali-activated slag paste (B). In the graphs, N and S indicate the weight percentage of Na<sub>2</sub>O and SiO<sub>2</sub> with respect  
636 to the precursor (slag, or blend of slag and fly ash), and B indicates blend of slag and fly ash. The curing temperature  
637 was 20 °C. The water to precursor ratio was 0.4.

638  
639 But at a later curing age, the pore solution of alkali-activated slag blended with fly ash paste had  
640 higher [Si] and lower [Na] than that of alkali-activated slag paste with the same alkaline  
641 activator. At 28 days (672 hours), the concentrations of Si and Na were 37.5 mmol/L and 1670.4  
642 mmol/L respectively in the pore solution of alkali-activated slag blended with fly ash paste, while  
643 they were 11.9 mmol/L and 2517.7 mmol/L respectively in the pore solution of alkali-activated  
644 slag paste. The higher [Si] in the alkali-activated slag blended with fly ash paste was because fly  
645 ash contains more reactive SiO<sub>2</sub> (37%) than slag (32.9%). The lower [Na] in the alkali-activated  
646 slag blended with fly ash paste was because the replacement of slag by fly ash led to the  
647 formation of alkali-aluminosilicate type gel. The alkali-aluminosilicate type gel was reported to

648 be formed together with calcium aluminosilicate type gel in alkali-activated blend of slag and fly  
649 ash in the literature [64, 71, 72]. The co-existence of calcium-aluminosilicate and alkali-  
650 aluminosilicate type gels was also confirmed by the solid phase analysis through XRD and FTIR.

651  
652 Figure 13(A) presents the XRD patterns of alkali-activated slag blended with fly ash and alkali-  
653 activated slag with the same alkaline activator, e.g. N6S5.4B in comparison with N6S5.4 at 28  
654 days. Like in alkali-activated slag paste (N6S5.4), calcium aluminosilicate hydrate was also  
655 formed in alkali-activated slag blended with fly ash paste. Since alkali-aluminosilicate type gel is  
656 amorphous to semi-crystalline [73], it was not detected by XRD. As such, FTIR technique was  
657 used to investigate the bonding environments in non-crystalline phases. Figure 13(B) plots the  
658 FTIR spectra of N6S5.4B and N6S5.4 at 28 days. The overall broad band of interest was located  
659 between 800 and 1200  $\text{cm}^{-1}$ . This band is associated with the asymmetric stretching mode of Si-  
660 O-T bonds (T: tetrahedral Si or Al), and is usually used to study the changes of the amorphous  
661 gel structure [74, 75]. The Si-O-T band was centered at 948  $\text{cm}^{-1}$  in alkali-activated slag paste,  
662 while it was centered at 952  $\text{cm}^{-1}$  in alkali-activated slag blended with fly ash paste. The shift of  
663 Si-O-T band towards to a higher wavenumber was attributed to the incorporation of fly ash that  
664 resulted in the formation of more crosslinked alkali-aluminosilicate type gel [64]. As such, it can  
665 be concluded that calcium aluminosilicate and alkali-aluminosilicate type gels were both formed  
666 in alkali-activated slag blended with fly ash paste (N6S5.4B).

667  
668 **Figure 13** Solid phase analysis of alkali-activated slag blended with fly ash and alkali-activated slag with the same  
669 alkaline activator: (A) X-ray patterns, and (B) FTIR spectra. In the graphs, Q, M, H, Ht, K and C-(N-)A-S-H refer to  
670 quartz, mullite, hematite, hydrotalcite, katoite and calcium aluminosilicate hydrate respectively, N and S indicate the

671 weight percentage of  $\text{Na}_2\text{O}$  and  $\text{SiO}_2$  with respect to the precursor (slag, or blend of slag and fly ash), and B indicates  
672 blend of slag and fly ash. The curing temperature was 20 °C. The water to precursor ratio was 0.4.

673  
674 Compared to the calcium aluminosilicate hydrate type gel, the alkali-aluminosilicate type gel  
675 takes up a larger amount of Na to balance the charge of Al in the bonding network [76]. As such,  
676 the pore solution of alkali-activated slag blended with fly ash paste had a relatively lower  
677 concentration of Na than that of alkali-activated slag paste with the same alkaline activator. The  
678 leaching of Na from AAMs is driven by the concentration gradients between the pore solution  
679 and the water that surrounds the materials [26]. From this point of view, the decreased  
680 concentration of Na in the pore solution due to the replacement of slag by fly ash can lead to  
681 decreases of the concentration gradients and thus reduce the leaching of Na in the alkali-activated  
682 slag blended with fly ash paste.

683  
684 3.5 Conceptual models to describe the elemental concentrations in the pore solutions of alkali-  
685 activated slag/fly ash pastes

686  
687 Figure 14(A) presents the conceptual model to describe the concentrations of Al, Ca, K, Fe, and  
688 Mg. Since Al, Ca, K, Fe and Mg are sourced from the precursor, the concentrations of these  
689 elements in the pore solution initially start from zero and increase with the progressive  
690 dissolution of the precursor. When the concentrations of these elements increase to be  
691 oversaturated with respect to solids, these elements are thermodynamically favored to precipitate  
692 and form the solids. If there are nuclei of the solids formed and the nuclei reach a critical size, the  
693 solids start to grow. The formation of nuclei and the growth of the solids consume the elements  
694 that constitute the solids. In the meantime, the dissolution of the precursor continues, releasing

695 these elements into the pore solution. When the consumption rates of these elements exceed the  
696 release rates of these elements, the concentrations of these elements decrease with time. Since the  
697 continuous release of these elements can partially compensate the consumption of these elements,  
698 the concentrations of these elements keep oversaturated with respect to the solids with time. But  
699 the degrees of oversaturation with respect to the solids decrease because the consumption of these  
700 elements cannot be completely replenished by the dissolution of the precursor.

701  
702 Since Si can be sourced from both the alkaline activator and the dissolution of the precursor, the  
703 conceptual model to describe the concentration of Si in the pore solution depends on the  
704 concentration of Si in the alkaline activator ( $[Si]_0$ ). If  $[Si]_0=0$  (Figure 14(B)), Si can only be  
705 sourced from the dissolution of the precursor and its concentration in the pore solution initially  
706 starts from zero and increase with the progressive dissolution of the precursor. When the release  
707 rate of Si is equal to the consumption rate of Si, the concentration of Si reaches the maximum  
708 concentration ( $[Si]_{max}$ ), after which it decreases with time. If  $0 < [Si]_0 < [Si]_{max}$  (Figure 14(C)), the  
709 concentration of Si in the pore solution initially starts from  $[Si]_0$ . Since  $[Si]_0 < [Si]_{max}$ , the release  
710 rate of Si from the precursor is larger than the consumption rate of Si. So, the concentration of Si  
711 increases with the progressive dissolution of the precursor until it reaches  $[Si]_{max}$ , at this point the  
712 release rate of Si from fly ash is equal to the consumption rate of Si, after which it decreases with  
713 time. If  $[Si]_0 \geq [Si]_{max}$  (Figure 14(D)), the concentration of Si in the pore solution initially starts  
714 from  $[Si]_0$  and decreases with time because the  $[Si]_0$  enables a consumption rate that is not  
715 smaller than the release rate of Si.

716

717 **Figure 14** Conceptual models to describe the concentrations of Al, Ca, K, Fe, Mg, Si, Na, OH<sup>-</sup> and S in the pore  
718 solution of alkali-activated slag/fly ash paste. In the graphs, [Si]<sub>0</sub> is the concentration of Si in the alkaline activator.  
719 [Si]<sub>max</sub> is the maximum concentration of Si.

720  
721 Figure 14(E) shows the conceptual model for the description of the concentrations of Na and OH<sup>-</sup>  
722 . Besides trace amount of Na<sub>2</sub>O in the precursors, Na in the pore solution is sourced from the  
723 alkaline activator. With the continuous formation of solids, for example the alkali-aluminosilicate  
724 type gel, the Na is consumed and thus the concentration of Na decreases with time. Although the  
725 dissolution of alkali-earth metals (Ca, Mg etc.) from the precursor may result in formation of  
726 hydroxyl ion in the pore solution, this amount of hydroxyl ions are much smaller than the amount  
727 consumed by the dissolution of Si and Al. So, the concentration of OH<sup>-</sup> decreases with time. S is  
728 sourced from slag/fly ash. Since no S related solids precipitate (as no S containing phases  
729 identified, see Figures 8, 11 and 13(A)), the concentration of S in the pore solution increases with  
730 time and reaches a maximum when S is completely dissolved from the precursor (Figure 14(F)).

731  
732 3.6 The influence of temperature on the pore solution composition of alkali-activated fly ash  
733 paste

734  
735 The increase of temperature led to decreases of the elemental concentrations in the pore solutions  
736 of alkali-activated fly ash pastes (see Figure 9). The influence of temperature on the pore solution  
737 composition of alkali-activated fly ash pastes can be discussed from the aspects of kinetics and  
738 thermodynamics.

739  
740 3.6.1 Kinetics

741  
742 The dissolution of fly ash releases the elements into the pore solution, while the formation of  
743 solid reaction products consumes the elements that constitute the solid reaction products. So, the  
744 elemental concentrations in the pore solution depend on the competition between the dissolution  
745 of fly ash and the formation of solid reaction products. The increase of temperature leads to  
746 accelerations of both the dissolution of fly ash and the formation of solid reaction products [77,  
747 78]. It means the increase of temperature accelerates both the release of elements from fly ash  
748 and the consumption of these elements by the formation of solid reaction products.

749  
750 Figure 15 plots the heat evolution rates of sodium hydroxide activated fly ash pastes at 40 °C and  
751 60 °C. The calorimetric responses of sodium silicate activated fly ash pastes show only one  
752 calorimetric peak (see Figure 10). This makes it impossible to separate the calorimetric response  
753 that corresponds to the dissolution of fly ash, and the calorimetric response that corresponds to  
754 the formation of alkali-aluminosilicate type gel. Thus, these results are not included in Figure 15.  
755 Comparing the calorimetric responses at 60 °C to the calorimetric responses at 40 °C, it can be  
756 seen that the increase of temperature led to a larger increase of the intensity of the second  
757 calorimetric peak. This indicates the increase of temperature had a larger acceleration of the  
758 formation of solid reaction products than that of the dissolution of fly ash.

759  
760 **Figure 15** Heat evolution rates of alkali-activated fly ash pastes at 40 °C (A) and 60 °C (B). In the graphs, P<sub>1</sub> and P<sub>2</sub>  
761 refer to the first and second calorimetric peak respectively, N and S indicate the weight percentage of Na<sub>2</sub>O and SiO<sub>2</sub>  
762 with respect to fly ash, and T indicates the curing temperature in Celsius. The water to fly ash ratio was 0.35.

763

764 Since the increase of temperature led to a larger acceleration of the consumption of elements than  
765 that of the release of elements, the consumption rates of elements exceed the release rates of  
766 elements at lower elemental concentrations. So, maximum elemental concentrations after the  
767 increase of temperature were smaller than the maximum concentrations before the increase of  
768 temperature. To show the influence of temperature on the pore solution composition of alkali-  
769 activated fly ash paste, Figure 16 plots the concentrations of Al, Ca, K, Fe and Mg before and  
770 after the increase of temperature. In the experiments, the alkali-activated fly ash pastes were in  
771 fluid state at the early curing time, which made it infeasible to collect the pore solution using the  
772 steel-die method. For this reason, the maximum elemental concentrations were not obtained. As  
773 shown in Figure 16, the experimental measurements started after the maximum elemental  
774 concentrations.

775  
776 **Figure 16** The influence of an increase of temperature on the concentrations of Al, Ca, K, Fe and Mg in the pore  
777 solution of alkali-activated fly ash paste.  $T_1$  and  $T_2$  are temperatures.

778

### 779 3.6.2 Thermodynamics

780

781 Thermodynamics assumes a solubility equilibrium between the solid and the aqueous species in  
782 the liquid that react to form the solid [17]. From this point of view, the solubility of the reaction  
783 products also influence the concentrations of the elements that react to form the solids. The  
784 alkali-aluminosilicate type gel, as the main solid reaction products in alkali-activated fly ash  
785 paste [79], is amorphous to semi-crystalline [73] and considered as the precursors to zeolites in  
786 the literature [75, 80]. It is reported that an increase of temperature leads to increase of long-  
787 range ordering and higher degree of crosslinking in alkali-aluminosilicate type gel [78, 81, 82].

788 This point can be further confirmed by the FTIR analysis. Figure 17 presents the infrared spectra  
789 of alkali-activated fly ash samples at 28 days. It can be observed that an increase of temperature  
790 (from 40 °C to 60 °C) led to the shift of the Si-O-T band to higher wavenumbers, from 971 to  
791 980  $\text{cm}^{-1}$  for sodium hydroxide activated fly ash and from 979 to 983  $\text{cm}^{-1}$  for sodium silicate  
792 activated fly ash. The shift of Si-O-T band from a lower wavenumber to a higher wavenumber  
793 indicates a higher degree of crosslinking of alkali-aluminosilicate type gel [64] and that the  
794 structure of alkali-aluminosilicate type gel becomes more ordered and stable [75]. As such, an  
795 increase of temperature leads to a higher degree of crosslinking of alkali-aluminosilicate type gel  
796 and a more stable structure.

797  
798 **Figure 17** FTIR spectra of alkali-activated fly ash samples at 28 days. In the graph, N and S indicate the weight  
799 percentage of  $\text{Na}_2\text{O}$  and  $\text{SiO}_2$  with respect to fly ash, and T indicates the curing temperature in Celsius. The water to  
800 fly ash ratio was 0.35.

801  
802 The higher degree of crosslinking and more stable structure of alkali-aluminosilicate type gel  
803 could lead to a decrease of the solubility of alkali-aluminosilicate type gel. The decreased  
804 solubility of alkali-aluminosilicate type gel results in lower concentrations of the elements that  
805 react to form the alkali-aluminosilicate type gel. So, the increase of temperature from 40 °C to 60  
806 °C led to decreases of the concentrations of Si, Al, Na and K that reacted to form alkali  
807 aluminosilicate type gel.

808

#### 809 **4 Conclusions**

810

811 This study investigated the pore solution composition of alkali-activated slag/fly ash pastes by  
812 means of ICP-OES analysis technique. The following conclusions can be drawn based on this  
813 study:

814

815 (1) In preparation of the samples for the ICP-OES analysis, alkaline dilution should be used  
816 for determination of the concentration of S. The acid dilution results in evaporation of  
817  $H_2S$  and white precipitation of S. In the pore solutions of alkali-activated slag/fly ash  
818 pastes, the elemental concentrations depend on the alkaline activator and curing  
819 temperature.

820

821 (2) The pore solutions of alkali-activated slag pastes are oversaturated with respect to solids.  
822 In the initial period, the effective saturation indexes with respect to calcium  
823 aluminosilicate hydrates are relatively high and decrease with time. On the contrary, the  
824 effective saturation indexes with respect to the crystalline phases increase rapidly. After  
825 the initial period, the effective saturation indexes show no substantial change with time.

826

827 (3) In the pore solutions of alkali-activated fly ash pastes, an increase of temperature leads to  
828 decreases of the concentrations of Si, Al, Ca, K, Fe and Mg, while the soluble silicate in  
829 the alkaline activator results in increases of these elemental concentrations.

830

831 (4) Compared to the alkali-activated slag paste with the same alkaline activator, 50 wt.%  
832 replacement of slag by fly ash does not result in a substantial influence on the pore  
833 solution composition of alkali-activated slag blended with fly ash paste.

834

835 (5) According to the experimental results, conceptual models are proposed to describe the  
836 elemental concentrations in the pore solutions. Based on the conceptual models, the  
837 influence of temperature on the pore solution composition of alkali-activated fly ash paste  
838 can be well interpreted. In addition, these conceptual models will help to develop kinetic  
839 models to describe quantitatively the developments of the elemental concentrations with  
840 time.

841

#### 842 **Acknowledgements**

843

844 The China Scholarship Council (the Grant Number 201406160048) and Microlab in Delft  
845 University of Technology are greatly acknowledged. The help by Mr. Shizhe Zhang on FTIR test  
846 is appreciated. The authors also would like to extend their grateful thanks to the anonymous  
847 reviewers, whose comments helped to substantially improve the quality of this paper.

848

#### 849 **Appendix. Pore solution composition data of alkali-activated slag/fly ash pastes**

850

851 The pore solution data, i.e. elemental concentrations of Si, Al, OH<sup>-</sup>, Ca, Na, K, Fe, Mg and S, are  
852 listed in Tables A1-A9.

853

854 **Table A1** Concentration of Si (mmol/L)

855

856 **Table A2** Concentration of Al (mmol/L)

857

858 **Table A3** Concentration of OH<sup>-</sup> (mmol/L)

859

860 **Table A4** Concentration of Ca (mmol/L)

861

862 **Table A5** Concentration of Na (mmol/L)

863

864 **Table A6** Concentration of K (mmol/L)

865

866 **Table A7** Concentration of Fe (mmol/L)

867

868 **Table A8** Concentration of Mg (mmol/L)

869

870 **Table A9** Concentration of S (mmol/L)

871

## 872 **References**

873

874 [1] J.L. Provis, S.A. Bernal, Geopolymers and related alkali-activated materials, *Annu. Rev. Mater. Res.*, 44 (2014)  
875 299-327.

876

877 [2] J.L. Provis, Alkali-activated materials, *Cem. Concr. Res.*, (2017).

878

879 [3] P. Duxson, J.L. Provis, G.C. Lukey, J.S. Van Deventer, The role of inorganic polymer technology in the  
880 development of 'green concrete', *Cem. Concr. Res.*, 37 (2007) 1590-1597.

881

882 [4] J.S. van Deventer, J.L. Provis, P. Duxson, D.G. Brice, Chemical research and climate change as drivers in the  
883 commercial adoption of alkali activated materials, *Waste and Biomass Valorization*, 1 (2010) 145-155.

884

885 [5] J.S.J. van Deventer, J.L. Provis, P. Duxson, Technical and commercial progress in the adoption of geopolymer  
886 cement, *Miner Eng.*, 29 (2012) 89-104.

887

888 [6] A. Fernández-Jiménez, J. Palomo, F. Puertas, Alkali-activated slag mortars: mechanical strength behaviour, Cem.  
889 Concr. Res., 29 (1999) 1313-1321.

890

891 [7] F. Pacheco-Torgal, Z. Abdollahnejad, A.F. Camões, M. Jamshidi, Y. Ding, Durability of alkali-activated binders:  
892 A clear advantage over Portland cement or an unproven issue?, Constr. Build. Mater., 30 (2012) 400-405.

893

894 [8] S.A. Bernal, J.L. Provis, Durability of Alkali- Activated Materials: Progress and Perspectives, J. Am. Ceram.  
895 Soc., 97 (2014) 997-1008.

896

897 [9] J. Miranda, A. Fernández-Jiménez, J. González, A. Palomo, Corrosion resistance in activated fly ash mortars,  
898 Cem. Concr. Res., 35 (2005) 1210-1217.

899

900 [10] C. Shi, Early hydration and microstructure development of alkali-activated slag cement pastes, Proceedings of  
901 the 10th International Congress on the Chemistry of Cement, Gothenburg, Sweden, 1997, pp. 3ii099.

902

903 [11] Z. Huanhai, W. Xuequan, X. Zhongzi, T. Mingshu, Kinetic study on hydration of alkali-activated slag, Cem.  
904 Concr. Res., 23 (1993) 1253-1258.

905

906 [12] A. Gruskovnjak, B. Lothenbach, L. Holzer, R. Figi, F. Winnefeld, Hydration of alkali-activated slag:  
907 comparison with ordinary Portland cement, Adv. Cem. Res., (2006) 119-128.

908

909 [13] M. Ben Haha, G. Le Saout, F. Winnefeld, B. Lothenbach, Influence of activator type on hydration kinetics,  
910 hydrate assemblage and microstructural development of alkali activated blast-furnace slags, Cem. Concr. Res., 41  
911 (2011) 301-310.

912

913 [14] B.S. Gebregziabihier, R.J. Thomas, S. Peethamparan, Temperature and activator effect on early-age reaction  
914 kinetics of alkali-activated slag binders, Constr. Build. Mater., 113 (2016) 783-793.

915

916 [15] Y. Ma, J. Hu, G. Ye, The effect of activating solution on the mechanical strength, reaction rate, mineralogy, and  
917 microstructure of alkali-activated fly ash, *J. Mater. Sci.*, 47 (2012) 4568-4578.

918

919 [16] D. Damidot, B. Lothenbach, D. Herfort, F.P. Glasser, Thermodynamics and cement science, *Cem. Concr. Res.*,  
920 41 (2011) 679-695.

921

922 [17] B. Lothenbach, Thermodynamic equilibrium calculations in cementitious systems, *Mater. Struct.*, 43 (2010)  
923 1413-1433.

924

925 [18] B. Lothenbach, D. Damidot, T. Matschei, J. Marchand, Thermodynamic modelling: State of knowledge and  
926 challenges, *Adv. Cem. Res.*, 22 (2010) 211-223.

927

928 [19] V.O. Ozçelik, C.E. White, Nanoscale Charge-Balancing Mechanism in Alkali-Substituted Calcium-Silicate-  
929 Hydrate Gels, *The journal of physical chemistry letters*, 7 (2016) 5266-5272.

930

931 [20] M. Criado, A. Fernández-Jiménez, A.G. de la Torre, M.A.G. Aranda, A. Palomo, An XRD study of the effect of  
932 the SiO<sub>2</sub>/Na<sub>2</sub>O ratio on the alkali activation of fly ash, *Cem. Concr. Res.*, 37 (2007) 671-679.

933

934 [21] D. Hobbs, Concrete deterioration: causes, diagnosis, and minimising risk, *International Materials Reviews*, 46  
935 (2001) 117-144.

936

937 [22] S. Mundra, M. Criado, S.A. Bernal, J.L. Provis, Chloride-induced corrosion of steel rebars in simulated pore  
938 solutions of alkali-activated concretes, *Cem. Concr. Res.*, 100 (2017) 385-397.

939

940 [23] S. Diamond, Particle morphologies in fly ash, *Cem. Concr. Res.*, 16 (1986) 569-579.

941

- 942 [24] S. Song, H.M. Jennings, Pore solution chemistry of alkali-activated ground granulated blast-furnace slag<sup>1</sup>, Cem.  
943 Concr. Res., 29 (1999) 159-170.  
944
- 945 [25] F. Puertas, A. Fernández-Jiménez, M.T. Blanco-Varela, Pore solution in alkali-activated slag cement pastes.  
946 Relation to the composition and structure of calcium silicate hydrate, Cem. Concr. Res., 34 (2004) 139-148.  
947
- 948 [26] R.R. Lloyd, J.L. Provis, J.S. Van Deventer, Pore solution composition and alkali diffusion in inorganic polymer  
949 cement, Cem. Concr. Res., 40 (2010) 1386-1392.  
950
- 951 [27] K. Scrivener, T. Füllmann, E. Gallucci, G. Walenta, E. Bermejo, Quantitative study of Portland cement  
952 hydration by X-ray diffraction/Rietveld analysis and independent methods, Cem. Concr. Res., 34 (2004) 1541-1547.  
953
- 954 [28] Y. Ma, Microstructure and Engineering Properties of Alkali Activated Fly Ash -as an environment friendly  
955 alternative to Portland cement, Tu Delft, Delft University of Technology, 2013.  
956
- 957 [29] W. Chen, H. Brouwers, The hydration of slag, part 1: reaction models for alkali-activated slag, J. Mater. Sci., 42  
958 (2007) 428-443.  
959
- 960 [30] A. Palomo, M.W. Grutzeck, M.T. Blanco, Alkali-activated fly ashes - A cement for the future, Cem. Concr.  
961 Res., 29 (1999) 1323-1329.  
962
- 963 [31] X. Gao, Q. Yu, H. Brouwers, Reaction kinetics, gel character and strength of ambient temperature cured alkali  
964 activated slag-fly ash blends, Constr. Build. Mater., 80 (2015) 105-115.  
965
- 966 [32] R.S. Barneyback Jr, S. Diamond, Expression and analysis of pore fluids from hardened cement pastes and  
967 mortars, Cem. Concr. Res., 11 (1981) 279-285.  
968

- 969 [33] B. Lothenbach, A. Gruskovnjak, Hydration of alkali-activated slag: thermodynamic modelling, *Adv. Cem. Res.*,  
970 19 (2007) 81-92.  
971
- 972 [34] D.A. Kulik, T. Wagner, S.V. Dmytrieva, G. Kosakowski, F.F. Hingerl, K.V. Chudnenko, U.R. Berner, GEM-  
973 Selektor geochemical modeling package: revised algorithm and GEMS3K numerical kernel for coupled simulation  
974 codes, *Comput. Geosci.*, 17 (2013) 1-24.  
975
- 976 [35] T. Wagner, D.A. Kulik, F.F. Hingerl, S.V. Dmytrieva, GEM-Selektor geochemical modeling package: TSolMod  
977 library and data interface for multicomponent phase models, *Can. Mineral.*, 50 (2012) 1173-1195.  
978
- 979 [36] R.J. Myers, S.A. Bernal, J.L. Provis, A thermodynamic model for C-(N-)A-S-H gel: CNASH-ss. Derivation and  
980 validation, *Cem. Concr. Res.*, 66 (2014) 27-47.  
981
- 982 [37] R.J. Myers, B. Lothenbach, S.A. Bernal, J.L. Provis, Thermodynamic modelling of alkali-activated slag  
983 cements, *Appl. Geochem.*, 61 (2015) 233-247.  
984
- 985 [38] A. C1679-14, Standard Practice for Measuring Hydration Kinetics of Hydraulic Cementitious Mixtures Using  
986 Isothermal Calorimetry, ASTM International, PA, West Conshohocken, 2014.  
987
- 988 [39] S. Ahmad, Reinforcement corrosion in concrete structures, its monitoring and service life prediction—a review,  
989 *Cem. Concr. Comp.*, 25 (2003) 459-471.  
990
- 991 [40] S.-Y. Hong, F.P. Glasser, Alkali sorption by C-S-H and C-A-S-H gels: Part II. Role of alumina, *Cem. Concr.*  
992 *Res.*, 32 (2002) 1101-1111.  
993
- 994 [41] E. L'Hôpital, B. Lothenbach, K. Scrivener, D. Kulik, Alkali uptake in calcium alumina silicate hydrate (CASH),  
995 *Cem. Concr. Res.*, 85 (2016) 122-136.  
996

- 997 [42] C. Shi, R. Day, Selectivity of alkaline activators for the activation of slags, Cement, Concrete and Aggregates,  
998 18 (1996) 8-14.  
999
- 1000 [43] D. Rothstein, J.J. Thomas, B.J. Christensen, H.M. Jennings, Solubility behavior of Ca-, S-, Al-, and Si-bearing  
1001 solid phases in Portland cement pore solutions as a function of hydration time, Cem. Concr. Res., 32 (2002) 1663-  
1002 1671.  
1003
- 1004 [44] S. Song, D. Sohn, H. Jennings, T. Mason, Hydration of alkali-activated ground granulated blast furnace slag, J.  
1005 Mater. Sci., 35 (2000) 249-257.  
1006
- 1007 [45] H.C. Helgeson, D.H. Kirkham, G.C. Flowers, Theoretical prediction of the thermodynamic behavior of aqueous  
1008 electrolytes by high pressures and temperatures; IV, Calculation of activity coefficients, osmotic coefficients, and  
1009 apparent molal and standard and relative partial molal properties to 600 degrees C and 5kb, American journal of  
1010 science, 281 (1981) 1249-1516.  
1011
- 1012 [46] K.S. Pitzer, Ion interaction approach: theory and data correlation, Activity coefficients in electrolyte solutions,  
1013 1991, pp. 75-153.  
1014
- 1015 [47] R.J. Myers, Thermodynamic Modelling of CaO-Al<sub>2</sub>O<sub>3</sub>-SiO<sub>2</sub>-H<sub>2</sub>O-Based Cements, University of Sheffield,  
1016 Sheffield, 2015.  
1017
- 1018 [48] R.J. Myers, S.A. Bernal, J.L. Provis, Phase diagrams for alkali-activated slag binders, Cem. Concr. Res., 95  
1019 (2017) 30-38.  
1020
- 1021 [49] C.J. Shi, R.L. Day, A Calorimetric Study of Early Hydration of Alkali-Slag Cements, Cem. Concr. Res., 25  
1022 (1995) 1333-1346.  
1023

- 1024 [50] S.-D. Wang, K.L. Scrivener, Hydration products of alkali activated slag cement, *Cem. Concr. Res.*, 25 (1995)  
1025 561-571.  
1026
- 1027 [51] I.G. Richardson, A.R. Brough, G.W. Groves, C.M. Dobson, The Characterization of Hardened Alkali-Activated  
1028 Blast-Furnace Slag Pastes and the Nature of the Calcium Silicate Hydrate (C-S-H) Phase, *Cem. Concr. Res.*, 24  
1029 (1994) 813-829.  
1030
- 1031 [52] H. Ye, A. Radlińska, Quantitative Analysis of Phase Assemblage and Chemical Shrinkage of Alkali-Activated  
1032 Slag, *J. Adv. Concr. Technol.*, 14 (2016) 245-260.  
1033
- 1034 [53] F. Bonk, J. Schneider, M.A. Cincotto, H. Panepucci, Characterization by multinuclear high-resolution NMR of  
1035 hydration products in activated blast-furnace slag pastes, *J. Am. Ceram. Soc.*, 86 (2003) 1712-1719.  
1036
- 1037 [54] M.B. Haha, B. Lothenbach, G. Le Saout, F. Winnefeld, Influence of slag chemistry on the hydration of alkali-  
1038 activated blast-furnace slag — Part I: Effect of MgO, *Cem. Concr. Res.*, 41 (2011) 955-963.  
1039
- 1040 [55] H.F. Taylor, *Cement chemistry*, Thomas Telford 1997.  
1041
- 1042 [56] J.E. Oh, P.J.M. Monteiro, S.S. Jun, S. Choi, S.M. Clark, The evolution of strength and crystalline phases for  
1043 alkali-activated ground blast furnace slag and fly ash-based geopolymers, *Cem. Concr. Res.*, 40 (2010) 189-196.  
1044
- 1045 [57] J.-L. Devidal, J. Schott, J.-L. Dandurand, An experimental study of kaolinite dissolution and precipitation  
1046 kinetics as a function of chemical affinity and solution composition at 150 C, 40 bars, and pH 2, 6.8, and 7.8,  
1047 *Geochim. Cosmochim. Acta*, 61 (1997) 5165-5186.  
1048
- 1049 [58] C.A. Rees, J.L. Provis, G.C. Lukey, J.S. van Deventer, The mechanism of geopolymer gel formation  
1050 investigated through seeded nucleation, *Colloids and Surfaces A: Physicochemical and Engineering Aspects*, 318  
1051 (2008) 97-105.

- 1052
- 1053 [59] E.H. Oelkers, General kinetic description of multioxide silicate mineral and glass dissolution, *Geochim.*  
1054 *Cosmochim. Acta*, 65 (2001) 3703-3719.
- 1055
- 1056 [60] R. Iler, Effect of adsorbed alumina on the solubility of amorphous silica in water, *J. Colloid Interface Sci.*, 43  
1057 (1973) 399-408.
- 1058
- 1059 [61] W.K.W. Lee, J.S.J. van Deventer, Structural reorganisation of class F fly ash in alkaline silicate solutions,  
1060 *Colloid Surface A*, 211 (2002) 49-66.
- 1061
- 1062 [62] S. Chithiraputhiran, N. Neithalath, Isothermal reaction kinetics and temperature dependence of alkali activation  
1063 of slag, fly ash and their blends, *Constr. Build. Mater.*, 45 (2013) 233-242.
- 1064
- 1065 [63] A. Fernández-Jiménez, F. Puertas, Effect of activator mix on the hydration and strength behaviour of alkali-  
1066 activated slag cements, *Adv. Cem. Res.*, 15 (2003) 129-136.
- 1067
- 1068 [64] I. Ismail, S.A. Bernal, J.L. Provis, R.S. Nicolas, S. Hamdan, J.S.J. van Deventer, Modification of phase  
1069 evolution in alkali-activated blast furnace slag by the incorporation of fly ash, *Cem. Concr. Comp.*, 45 (2014) 125-  
1070 135.
- 1071
- 1072 [65] I. García-Lodeiro, A. Fernández-Jiménez, A. Palomo, D.E. Macphee, Effect of calcium additions on N–A–S–H  
1073 cementitious gels, *J. Am. Ceram. Soc.*, 93 (2010) 1934-1940.
- 1074
- 1075 [66] A. Fernandez-Jimenez, A. Palomo, I. Sobrados, J. Sanz, The role played by the reactive alumina content in the  
1076 alkaline activation of fly ashes, *Micropor Mesopor Mat*, 91 (2006) 111-119.
- 1077
- 1078 [67] M. Criado, A. Fernández-Jiménez, A. Palomo, I. Sobrados, J. Sanz, Effect of the SiO<sub>2</sub>/Na<sub>2</sub>O ratio on the alkali  
1079 activation of fly ash. Part II: <sup>29</sup>Si MAS-NMR Survey, *Micropor Mesopor Mat*, 109 (2008) 525-534.

- 1080
- 1081 [68] A. Fernández-Jiménez, A. Palomo, M. Criado, Alkali activated fly ash binders. A comparative study between  
1082 sodium and potassium activators, *Mater Construcc*, 56 (2006) 51-65.
- 1083
- 1084 [69] J. Davidovits, *Geopolymers, Journal of thermal analysis*, 37 (1991) 1633-1656.
- 1085
- 1086 [70] C.B. Cheah, W.K. Part, M. Ramli, The hybridizations of coal fly ash and wood ash for the fabrication of low  
1087 alkalinity geopolymer load bearing block cured at ambient temperature, *Constr. Build. Mater.*, 88 (2015) 41-55.
- 1088
- 1089 [71] S.A. Bernal, J.L. Provis, B. Walkley, R. San Nicolas, J.D. Gehman, D.G. Brice, A.R. Kilcullen, P. Duxson, J.S.  
1090 van Deventer, Gel nanostructure in alkali-activated binders based on slag and fly ash, and effects of accelerated  
1091 carbonation, *Cem. Concr. Res.*, 53 (2013) 127-144.
- 1092
- 1093 [72] S. Puligilla, P. Mondal, Co-existence of aluminosilicate and calcium silicate gel characterized through selective  
1094 dissolution and FTIR spectral subtraction, *Cem. Concr. Res.*, 70 (2015) 39-49.
- 1095
- 1096 [73] J. Davidovits, *Geopolymers: inorganic polymeric new materials, Journal of Thermal Analysis and calorimetry*,  
1097 37 (1991) 1633-1656.
- 1098
- 1099 [74] C.A. Rees, J.L. Provis, G.C. Lukey, J.S. Van Deventer, In situ ATR-FTIR study of the early stages of fly ash  
1100 geopolymer gel formation, *Langmuir*, 23 (2007) 9076-9082.
- 1101
- 1102 [75] M. Criado, A. Fernández-Jiménez, A. Palomo, Alkali activation of fly ash: Effect of the SiO<sub>2</sub>/Na<sub>2</sub>O ratio: Part  
1103 I: FTIR study, *Micropor Mesopor Mat*, 106 (2007) 180-191.
- 1104
- 1105 [76] M.R. Rowles, B.H. O'Connor, Chemical and structural microanalysis of aluminosilicate geopolymers  
1106 synthesized by sodium silicate activation of metakaolinite, *J. Am. Ceram. Soc.*, 92 (2009) 2354-2361.
- 1107

1108 [77] D. Hardjito, B.V. Rangan, Development and properties of low-calcium fly ash-based geopolymer concrete,  
1109 Curtin University of Technology, 2005.

1110  
1111 [78] P. Duxson, A. Fernández-Jiménez, J. Provis, G. Lukey, A. Palomo, J. Van Deventer, Geopolymer technology:  
1112 the current state of the art, J. Mater. Sci., 42 (2007) 2917-2933.

1113  
1114 [79] A. Fernández-Jiménez, A. Palomo, Composition and microstructure of alkali activated fly ash binder: effect of  
1115 the activator, Cem. Concr. Res., 35 (2005) 1984-1992.

1116  
1117 [80] J.L. Provis, J.S.J. Van Deventer, Geopolymers: structures, processing, properties and industrial applications,  
1118 Elsevier 2009.

1119  
1120 [81] R. Barrer, D. Mainwaring, Chemistry of soil minerals. Part XIII. Reactions of metakaolinite with single and  
1121 mixed bases, Journal of the Chemical Society, Dalton Transactions, (1972) 2534-2546.

1122  
1123 [82] C.E. White, J.L. Provis, T. Proffen, J.S. Van Deventer, The effects of temperature on the local structure of  
1124 metakaolin-based geopolymer binder: A neutron pair distribution function investigation, J. Am. Ceram. Soc., 93  
1125 (2010) 3486-3492.

1126

1127

1128

1129

1130

1131

1132

1133

1134 **Tables**

1135

1136 **Table 1** Chemical compositions of blast furnace slag and fly ash (by weight, %)

Oxide	SiO <sub>2</sub>	CaO	Al <sub>2</sub> O <sub>3</sub>	MgO	Fe <sub>2</sub> O <sub>3</sub>	SO <sub>3</sub>	K <sub>2</sub> O	TiO <sub>2</sub>	L.I.*
Slag	32.91	40.96	11.85	9.23	0.46	1.61	0.33	1.00	1.15
Fly ash	52.90	4.36	26.96	1.50	6.60	0.73	1.31	1.14	3.37

1137 \*L.I. refers to loss on ignition.

1138

1139

1140

1141 **Table 2** Mixture compositions and curing temperature

Sample <sup>a</sup>	Precursor	Na <sub>2</sub> O <sup>b</sup>	SiO <sub>2</sub> <sup>b</sup>	Curing temperature
N4S0	slag	4	0	20 °C
N6S0	slag	6	0	20 °C
N8S0	slag	8	0	20 °C
N4S2.7	slag	4	2.7	20 °C
N4S5.4	slag	4	5.4	20 °C
N6S5.4	slag	6	5.4	20 °C
N8S5.4	slag	8	5.4	20 °C
N6.2S0T40	fly ash	6.2	0	40 °C
N9.3S0T40	fly ash	9.3	0	40 °C
N9.3S9T40	fly ash	9.3	9	40 °C
N6.2S0T60	fly ash	6.2	0	60 °C
N9.3S0T60	fly ash	9.3	0	60 °C
N9.3S9T60	fly ash	9.3	9	60 °C
N6S5.4B	blend <sup>c</sup>	6	5.4	20 °C

1142 <sup>a</sup>N and S indicates weight percentage of Na<sub>2</sub>O and SiO<sub>2</sub> with respect to precursor, T indicates temperature in Celsius

1143 and B indicates blend of slag and fly ash.

1144 <sup>b</sup>weight percentage with respect to precursor content (wt. %).1145 <sup>c</sup>blend = 50 wt. % slag + 50 wt. % fly ash.

1146

1147

1148

1149

1150

1151

1152 **Table 3** The pH and concentrations of Na, Si, and OH<sup>-</sup> in the alkaline activators

Sample <sup>a</sup>	pH	[Na] (mmol/L)	[Si] (mmol/L)	[OH <sup>-</sup> ] (mmol/L) <sup>b</sup>
N4S0	14.31	3239	0	3239(1957)
N6S0	14.50	4857	0	4857(2517)
N8S0	14.64	6466	0	6466(2953)
N4S2.7	14.14	3204	1117	1757(831)
N4S5.4	13.87	3193	2227	821(261)
N6S5.4 and N6S5.4B	14.30	4773	2219	2218(578)
N8S5.4	14.52	6339	2211	3636(817)
N6.2S0T40 and N6.2S0T60	14.58	5731	0	5731(2766)
N9.3S0T40 and N9.3S0T60	14.79	8564	0	8564(3408)
N9.3S9T40 and N9.3S9T60	14.60	8340	4170	3908(257)

1153 <sup>a</sup>N and S indicates weight percentage of Na<sub>2</sub>O and SiO<sub>2</sub> with respect to precursor, T indicates temperature in Celsius

1154 and B indicates blend of slag and fly ash.

1155 <sup>b</sup>The numbers outside the brackets were obtained by thermodynamic calculations including the hydroxide from

1156 NaOH(aq), while those inside the brackets were obtained by excluding the hydroxide from NaOH(aq).

1157

1158

1159 **Table 4** Chemical reactions and equilibrium solubility products at 25°C and 1 bar for eight end-members and

1160 crystalline reaction products in alkali-activated slag

End-member	Chemical reactions	Log K <sub>30</sub>
<i>C-(N)-A-S-H gel ideal solid solution eight end-members, 'CNASH_ss' model [36]</i>		
5CA	(CaO) <sub>1.25</sub> ·(Al <sub>2</sub> O <sub>3</sub> ) <sub>0.125</sub> ·(SiO <sub>2</sub> )·(H <sub>2</sub> O) <sub>1.625</sub> ⇌ 1.25Ca <sup>2+</sup> + SiO <sub>3</sub> <sup>2-</sup> + 0.25AlO <sub>2</sub> <sup>-</sup> + 0.25OH <sup>-</sup> + 1.5H <sub>2</sub> O	-10.75
INFCA	(CaO)·(Al <sub>2</sub> O <sub>3</sub> ) <sub>0.15625</sub> ·(SiO <sub>2</sub> ) <sub>1.1875</sub> ·(H <sub>2</sub> O) <sub>1.65625</sub> + 0.6875OH <sup>-</sup> ⇌ Ca <sup>2+</sup> + 1.1875SiO <sub>3</sub> <sup>2-</sup> + 0.3125AlO <sub>2</sub> <sup>-</sup> + 2H <sub>2</sub> O	-8.90
5CNA	(CaO) <sub>1.25</sub> ·(Na <sub>2</sub> O) <sub>0.25</sub> ·(Al <sub>2</sub> O <sub>3</sub> ) <sub>0.125</sub> ·(SiO <sub>2</sub> )·(H <sub>2</sub> O) <sub>1.25</sub> ⇌ 1.25Ca <sup>2+</sup> + SiO <sub>3</sub> <sup>2-</sup> + 0.25AlO <sub>2</sub> <sup>-</sup> + 0.5Na <sup>+</sup> + 0.75OH <sup>-</sup> + H <sub>2</sub> O	-10.40
INFCNA	(CaO)·(Na <sub>2</sub> O) <sub>0.34375</sub> ·(Al <sub>2</sub> O <sub>3</sub> ) <sub>0.15625</sub> ·(SiO <sub>2</sub> ) <sub>1.1875</sub> ·(H <sub>2</sub> O) <sub>1.3</sub> ⇌ Ca <sup>2+</sup> + 1.1875SiO <sub>3</sub> <sup>2-</sup> + 0.3125AlO <sub>2</sub> <sup>-</sup> + 0.6875Na <sup>+</sup> + 1.3125H <sub>2</sub> O	-10.00
INFCN	(CaO)·(Na <sub>2</sub> O) <sub>0.3125</sub> ·(SiO <sub>2</sub> ) <sub>1.5</sub> ·(H <sub>2</sub> O) <sub>1.1875</sub> + 0.375OH <sup>-</sup> ⇌ Ca <sup>2+</sup> + 1.5SiO <sub>3</sub> <sup>2-</sup> + 0.625Na <sup>+</sup> + 1.375H <sub>2</sub> O	-10.70
T2C*	(CaO) <sub>1.5</sub> ·(SiO <sub>2</sub> )·(H <sub>2</sub> O) <sub>2.5</sub> ⇌ 1.5Ca <sup>2+</sup> + SiO <sub>3</sub> <sup>2-</sup> + OH <sup>-</sup> + 2H <sub>2</sub> O	-11.60
T5C*	(CaO) <sub>1.25</sub> ·(SiO <sub>2</sub> ) <sub>1.25</sub> ·(H <sub>2</sub> O) <sub>2</sub> ⇌ 1.25Ca <sup>2+</sup> + 1.25SiO <sub>3</sub> <sup>2-</sup> + 2.5H <sub>2</sub> O	-10.50
TobH*	(CaO)·(SiO <sub>2</sub> ) <sub>1.5</sub> ·(H <sub>2</sub> O) <sub>2.5</sub> + OH <sup>-</sup> ⇌ Ca <sup>2+</sup> + 1.5SiO <sub>3</sub> <sup>2-</sup> + 3H <sub>2</sub> O	-7.90
<i>Crystalline reaction products in alkali-activated slag [17, 33]</i>		
C <sub>2</sub> ASH <sub>8</sub>	(CaO) <sub>2</sub> ·(Al <sub>2</sub> O <sub>3</sub> )·(SiO <sub>2</sub> )·(H <sub>2</sub> O) <sub>8</sub> ⇌ 2Ca <sup>2+</sup> + 2AlO <sub>2</sub> <sup>-</sup> + SiO <sub>3</sub> <sup>2-</sup> + 8H <sub>2</sub> O	-19.10
C <sub>3</sub> AH <sub>6</sub>	(CaO) <sub>3</sub> ·(Al <sub>2</sub> O <sub>3</sub> )·(H <sub>2</sub> O) <sub>6</sub> ⇌ 3Ca <sup>2+</sup> + 2AlO <sub>2</sub> <sup>-</sup> + 4OH <sup>-</sup> + 4H <sub>2</sub> O	-20.85
Ca(OH) <sub>2</sub>	Ca(OH) <sub>2</sub> ⇌ Ca <sup>2+</sup> + 2OH <sup>-</sup>	-5.20
C <sub>4</sub> AH <sub>13</sub>	(CaO) <sub>4</sub> ·(Al <sub>2</sub> O <sub>3</sub> )·(H <sub>2</sub> O) <sub>13</sub> ⇌ 4Ca <sup>2+</sup> + 2AlO <sub>2</sub> <sup>-</sup> + 6OH <sup>-</sup> + 10H <sub>2</sub> O	-25.41

1161

1162

1163

1164 **Table A1** Concentration of Si (mmol/L)

Sample	Time (hours)						
	3	7	24	72	168	336	672
N4S0	24.9	17.9	9.6	5.9	4.6	4.5	3.7
N6S0	39.7	33.7	22.3	14.3	11.5	9.1	7.7
N8S0	44.6	45.7	42.2	27.4	21.4	18.4	16.3
N4S2.7	-- <sup>a</sup>	--	13.6	7.6	6.1	5.5	5.1
N4S5.4	469.6	312.9	22.4	12.1	9.7	7.5	6.4
N6S5.4	172.6	40.9	29.0	18.4	15.6	13.6	11.9
N8S5.4	78.9	67.1	50.9	38.2	30.9	28.6	25.7
N6.2S0T40	--	--	--	990.9	922.5	--	219.1
N9.3S0T40	--	--	--	2123.4	1048.0	--	150.2
N9.3S9T40	--	--	--	1965.9	2089.6	--	1381.3
N6.2S0T60	--	--	1107.3	374.3	113.6	--	12.8
N9.3S0T60	--	--	1504.5	552.1	221.6	--	74
N9.3S9T60	--	--	2421.6	2043.6	1787.7	--	655.6
N6S5.4B	--	227.9	63.8	56.5	37.5	--	37.5

1165 <sup>a</sup>-- means not measured.

1166

1167 **Table A2** Concentration of Al (mmol/L)

Sample	Time (hours)						
	3	7	24	72	168	336	672
N4S0	10.3	10.2	9.7	8.8	8.4	7.9	7.5
N6S0	15.4	15.4	15.1	14.6	14.2	12.4	12.1
N8S0	24.4	23.3	22.9	21.6	20.4	19.5	19.1
N4S2.7	-- <sup>a</sup>	--	15.7	15.4	14.4	14.4	13.3
N4S5.4	11.8	10.8	9.7	12.2	13.2	12.4	11.1
N6S5.4	17.3	23.3	22.3	22.1	21.7	20.6	18.9
N8S5.4	32.7	32.3	32.9	32.3	30.7	31.3	29.3
N6.2S0T40	--	--	--	41.7	22.7	--	2.0
N9.3S0T40	--	--	--	177.8	32.8	--	1.1
N9.3S9T40	--	--	--	207.9	144.0	--	12.8
N6.2S0T60	--	--	26.9	3.1	0.3	--	--
N9.3S0T60	--	--	35.8	4.4	1.0	--	0.3
N9.3S9T60	--	--	128.0	36.9	15.9	--	2.3
N6S5.4B	--	21.4	30.9	29.7	30.1	--	25.4

1168 <sup>a</sup>-- means not measured.

1169

1170

1171

1172

1173

1174

1175

1176 **Table A3** Concentration of OH<sup>-</sup> (mmol/L)

Sample	Time (hours)						
	3	7	24	72	168	336	672
N4S0	2098	2153	1890	1667	1581	1410	1289
N6S0	2907	3145	2864	2640	2537	2468	2213
N8S0	4149	4076	3989	3910	3883	3572	3621
N4S2.7	-- <sup>a</sup>	--	1372	1070	1100	1009	969
N4S5.4	--	--	833	783	803	702	589
N6S5.4	2251	2074	1882	1747	1550	1426	1270
N8S5.4	2926	2941	2695	2609	2478	2406	2163
N6.2S0T40	--	--	--	2525	1015	--	333
N9.3S0T40	--	--	--	--	2327	--	1177
N9.3S9T40	--	--	--	--	1292	--	424
N6.2S0T60	--	--	1223	432	218	--	119
N9.3S0T60	--	--	2295	1643	1290	--	628
N9.3S9T60	--	--	1486	610	250	--	202
N6S5.4B	--	2370	--	--	--	--	1128

1177 <sup>a</sup>-- means not measured.

1178

1179 **Table A4** Concentration of Ca (mmol/L)

Sample	Time (hours)						
	3	7	24	72	168	336	672
N4S0	0.64	0.58	0.63	0.66	0.67	0.81	0.76
N6S0	0.53	0.47	0.36	0.53	0.58	0.52	0.57
N8S0	0.59	0.56	0.51	0.44	0.59	0.56	0.54
N4S2.7	-- <sup>a</sup>	--	0.32	0.32	0.34	0.35	0.39
N4S5.4	2.34	--	1.49	1.40	1.24	1.28	1.56
N6S5.4	0.58	0.46	0.51	0.49	0.60	0.65	0.75
N8S5.4	0.50	0.40	0.35	0.35	0.36	0.26	0.23
N6.2S0T40	--	--	--	4.05	2.83	--	1.52
N9.3S0T40	--	--	--	12.23	3.80	--	1.10
N9.3S9T40	--	--	--	17.23	16.1	--	1.67
N6.2S0T60	--	--	2.33	1.10	0.69	--	0.99
N9.3S0T60	--	--	2.70	0.98	0.61	--	0.71
N9.3S9T60	--	--	11.18	3.93	1.78	--	0.98
N6S5.4B	--	0.71	1.16	0.69	0.56	--	1.02

1180 <sup>a</sup>-- means not measured.

1181

1182

1183

1184

1185

1186

1187

1188 **Table A5** Concentration of Na (mmol/L)

Sample	Time (hours)						
	3	7	24	72	168	336	672
N4S0	2793	2729	2459	2184	2141	1948	1747
N6S0	4064	4231	3956	3606	3518	3467	3077
N8S0	6291	5542	5948	5722	5162	5374	5207
N4S2.7	-- <sup>a</sup>	--	1994	1879	1862	1802	1735
N4S5.4	2436	2254	1426	1386	1508	1387	1343
N6S5.4	3252	3136	3007	2750	2664	2600	2518
N8S5.4	4370	4322	4160	4104	4149	4122	3774
N6.2S0T40	--	--	--	3990	2268	--	1323
N9.3S0T40	--	--	--	5287	3191	--	1680
N9.3S9T40	--	--	--	4450	3802	--	2155
N6.2S0T60	--	--	2489	1335	1027	--	792
N9.3S0T60	--	--	3117	2071	1651	--	1443
N9.3S9T60	--	--	3669	2612	2395	--	1631
N6S5.4B	--	3921	3189	2804	2515	--	1670

1189 <sup>a</sup>-- means not measured.

1190

1191 **Table A6** Concentration of K (mmol/L)

Sample	Time (hours)						
	3	7	24	72	168	336	672
N4S0	30.7	39.7	52.6	61.7	72.2	77.7	81.2
N6S0	40.6	53.6	65.4	83.0	98.6	109.8	124.5
N8S0	57.9	60.6	72.4	87.4	105.4	120.9	139.9
N4S2.7	-- <sup>a</sup>	--	33.0	44.3	48.4	54.6	56.9
N4S5.4	7.6	8.5	15.7	26.0	33.6	32.8	35.4
N6S5.4	16.5	41.1	45.9	56.1	62.3	67.0	62.2
N8S5.4	52.0	56.7	68.1	78.3	88.5	94.9	93.2
N6.2S0T40	--	--	--	88.4	61.5	--	26.4
N9.3S0T40	--	--	--	81.9	49.0	--	24.9
N9.3S9T40	--	--	--	126.4	115.4	--	50.8
N6.2S0T60	--	--	56.6	22.5	14.8	--	9.8
N9.3S0T60	--	--	39.6	23.7	16.1	--	13.5
N9.3S9T60	--	--	104.0	59.5	49.9	--	24.4
N6S5.4B	--	20.0	37.2	46.4	50.7	--	44.1

1192 <sup>a</sup>-- means not measured.

1193

1194 **Table A7** Concentration of Fe (mmol/L)

Sample	Time (hours)			
	24	72	168	672
N6.2S0T40	-- <sup>a</sup>	1.72	1.11	0.12
N9.3S0T40	--	9.05	1.49	--
N9.3S9T40	--	12.46	8.64	0.32
N6.2S0T60	0.88	0.15	--	--
N9.3S0T60	1.30	0.13	--	--
N9.3S9T60	4.375	1.55	0.52	0.20

1195 <sup>a</sup>-- means not measured.

1196

1197 **Table A8** Concentration of Mg (mmol/L)

Sample	Time (hours)			
	24	72	168	672
N6.2S0T40	-- <sup>a</sup>	1.58	1.29	0.19
N9.3S0T40	--	8.04	1.19	0.09
N9.3S9T40	--	9.29	7.92	0.39
N6.2S0T60	0.75	0.13	--	--
N9.3S0T60	0.92	0.11	--	0.06
N9.3S9T60	3.83	1.21	1.42	0.18

1198 <sup>a</sup>-- means not measured.

1199

1200 **Table A9** Concentration of S (mmol/L)

Sample	Time (hours)			
	24	72	168	672
N6.2S0T40	-- <sup>a</sup>	253	274	356
N9.3S0T40	--	345	367	449
N9.3S9T40	--	40	47	63
N6.2S0T60	238	287	339	317
N9.3S0T60	315	360	371	391
N9.3S9T60	20	25	25	40

1201 <sup>a</sup>-- means not measured.

1202

1203

1204

1205

1206

1207

1208

1209

1210

1211

1212

1213

1214

1215

1216 **Figures**

1217

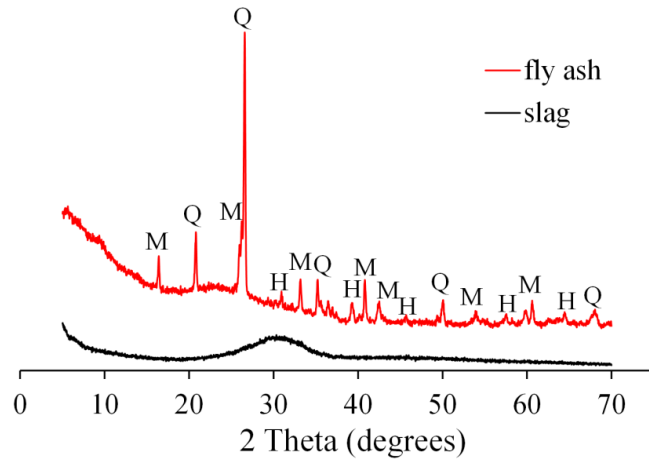


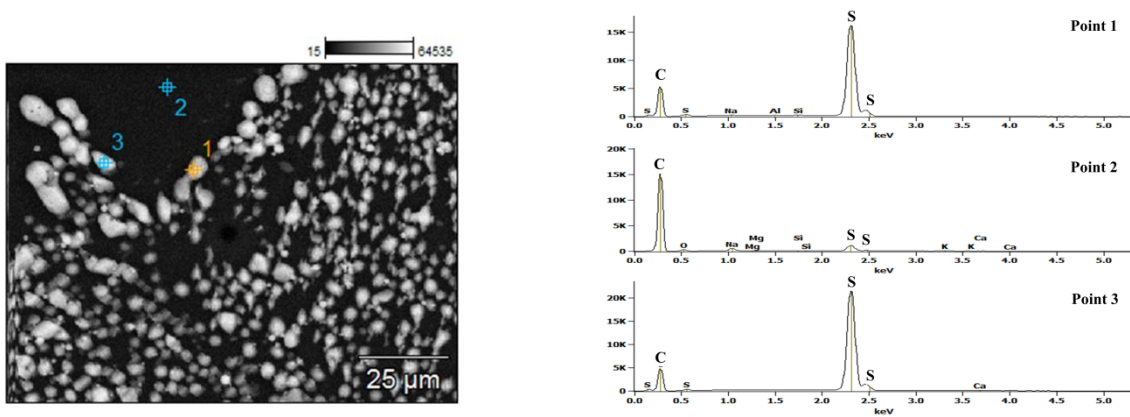
**Figure 1** X-ray diffraction patterns of slag and fly ash. In the graph, Q, M and H refer to quartz, mullite and hematite respectively.

1218

1219

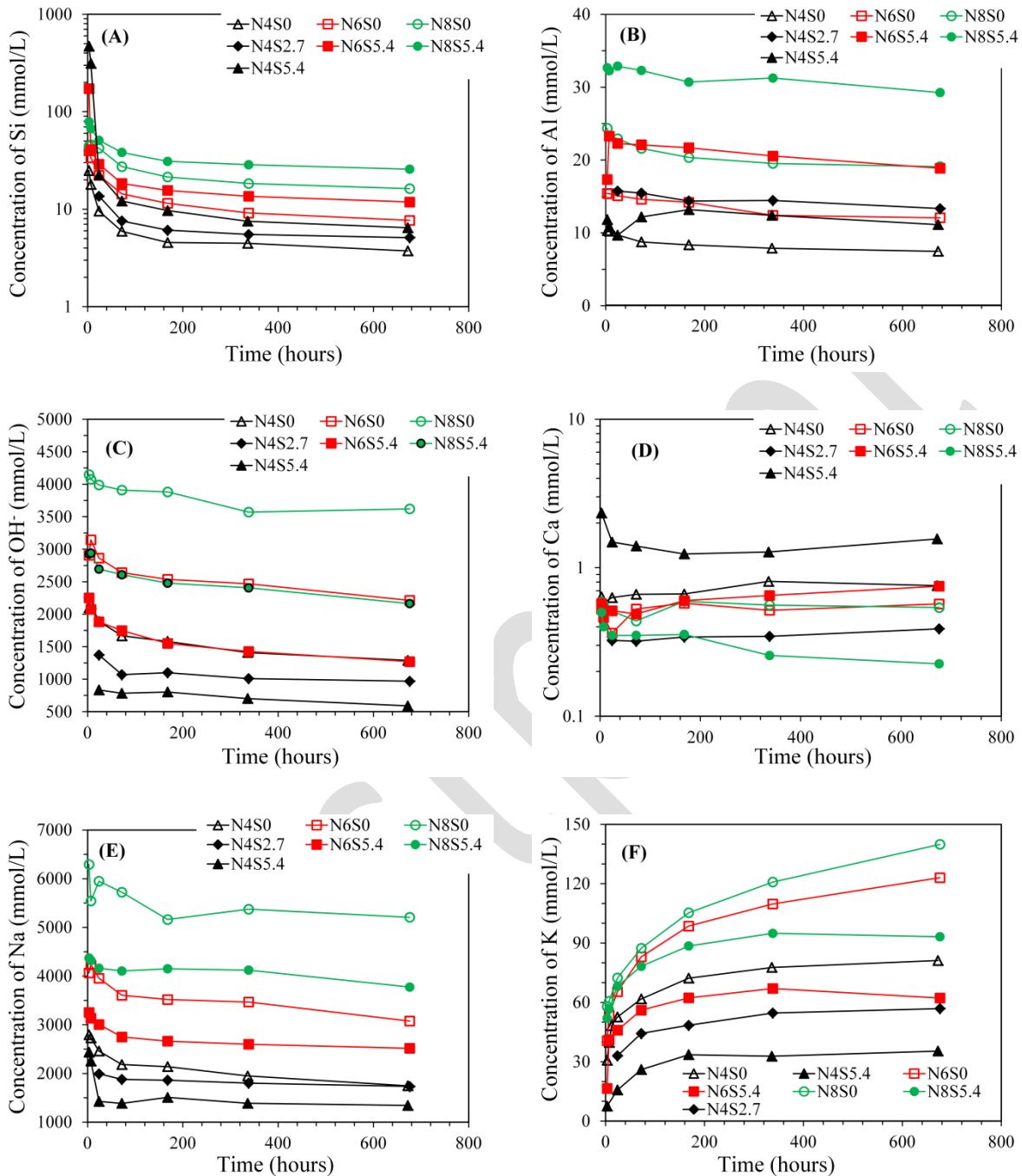
1220

1221



**Figure 2** White precipitation and its element composition in diluted pore solution using nitric acid.

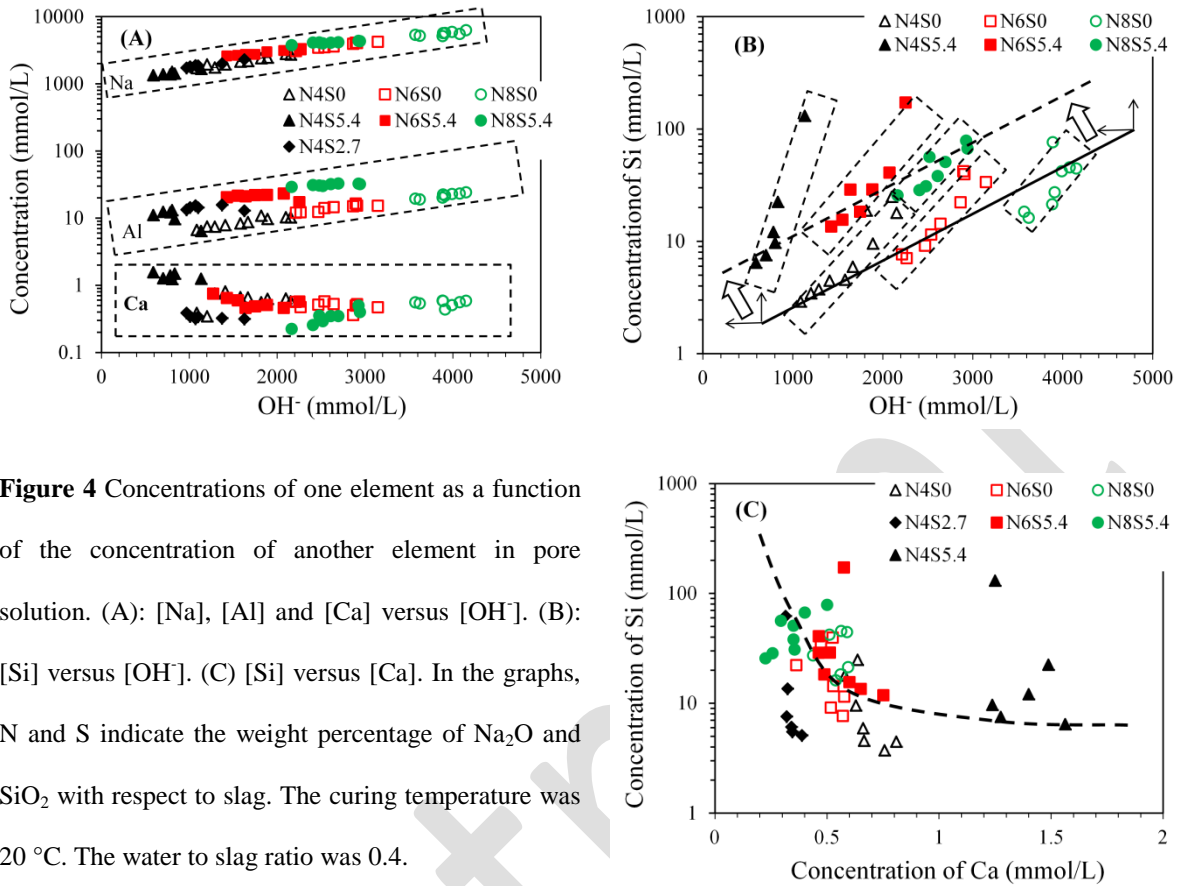
1222



**Figure 3** Elemental concentrations in the pore solutions of alkali-activated slag pastes. In the graphs, N and S indicate weight percentage of Na<sub>2</sub>O and SiO<sub>2</sub> with respect to slag. The water to slag ratio was 0.4 and the curing temperature was 20 °C.

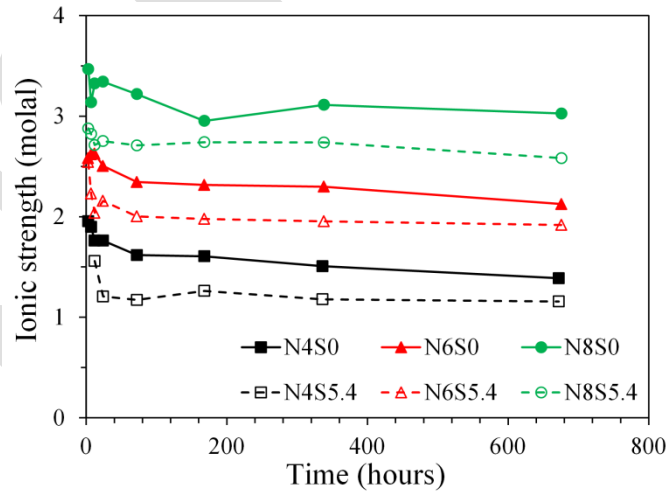
1223

1224

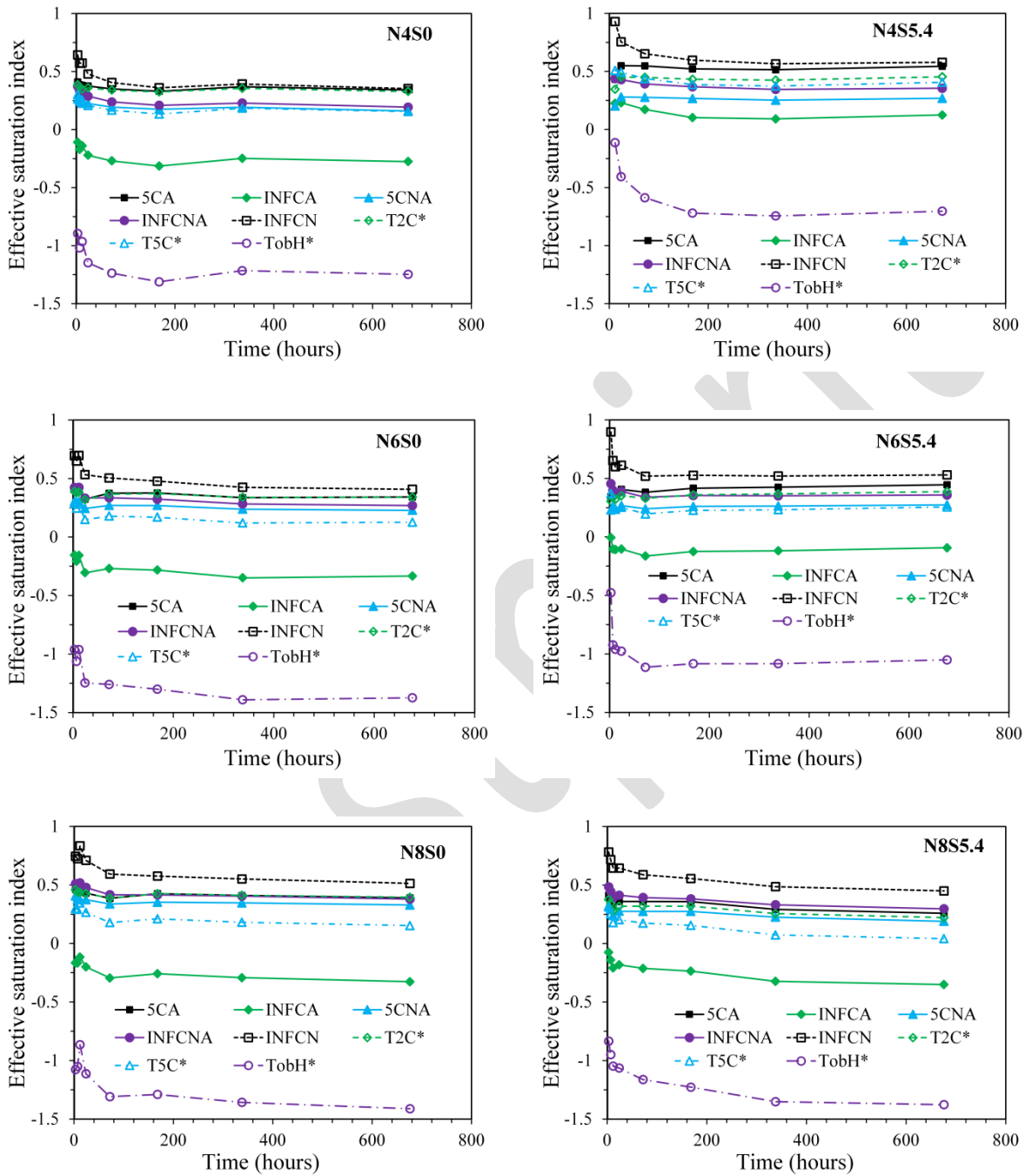


**Figure 4** Concentrations of one element as a function of the concentration of another element in pore solution. (A): [Na], [Al] and [Ca] versus [OH<sup>-</sup>]. (B): [Si] versus [OH<sup>-</sup>]. (C) [Si] versus [Ca]. In the graphs, N and S indicate the weight percentage of Na<sub>2</sub>O and SiO<sub>2</sub> with respect to slag. The curing temperature was 20 °C. The water to slag ratio was 0.4.

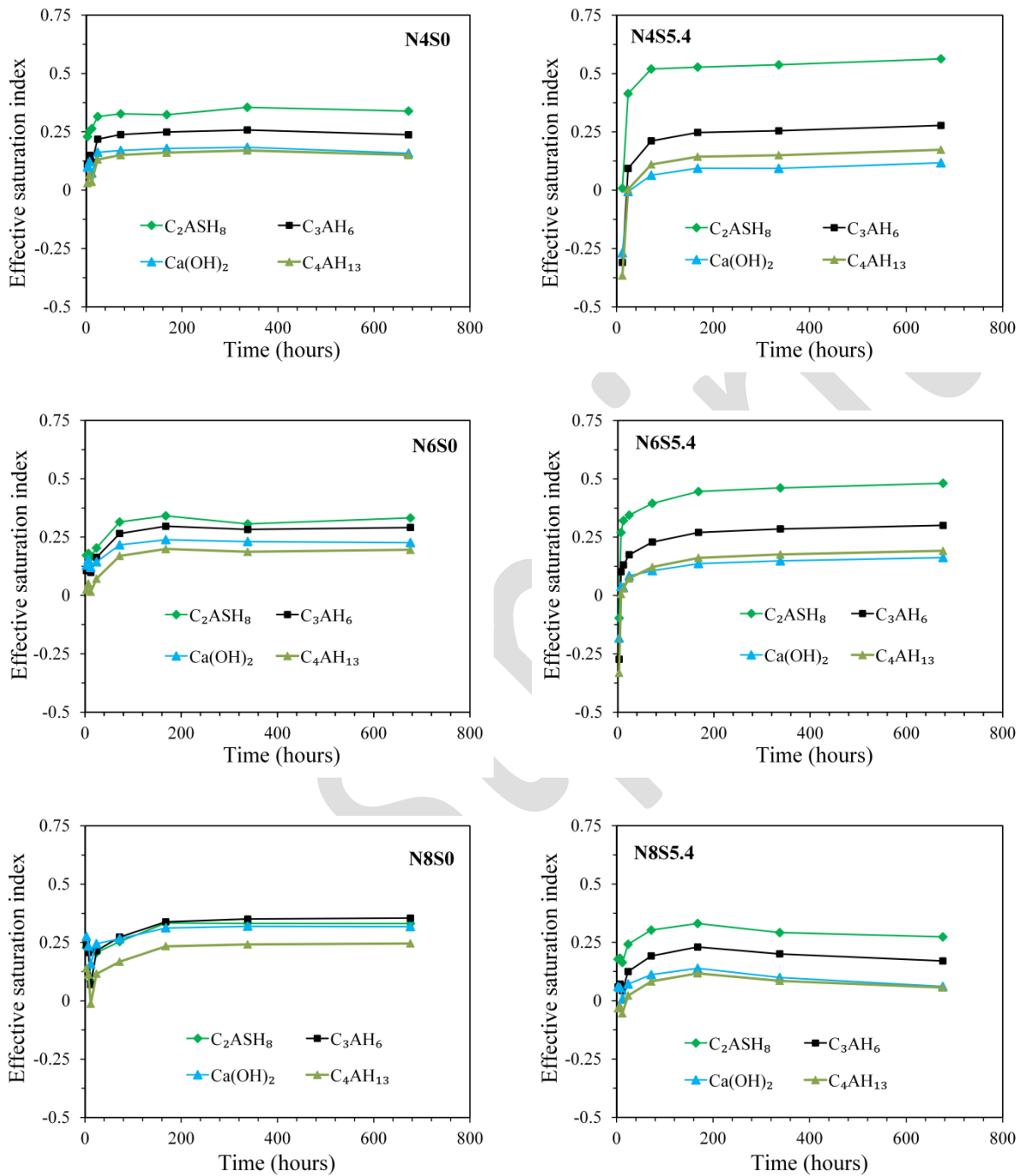
1225



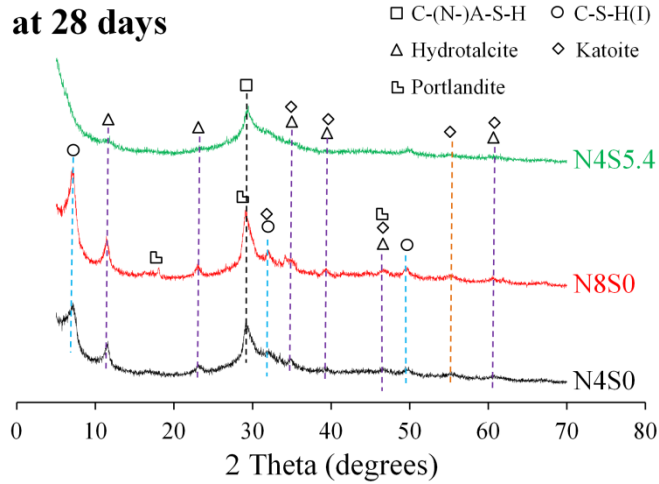
**Figure 5** The ionic strengths in the pore solutions of alkali-activated slag pastes, calculated by GEM-Selektor. In the graphs, N and S indicate the weight percentage of Na<sub>2</sub>O and SiO<sub>2</sub> with respect to slag. The curing temperature was 20 °C. The water to slag ratio was 0.4.



**Figure 6** Effective saturation indexes with respect to the eight end-members as functions of time. In the graphs, N and S indicate the weight percentage of  $\text{Na}_2\text{O}$  and  $\text{SiO}_2$  with respect to slag. The curing temperature was 20 °C. The water to slag ratio was 0.4. A ESI of 0 indicates equilibrium between solution and solid; a positive ESI indicates oversaturation and a negative ESI indicates undersaturation.

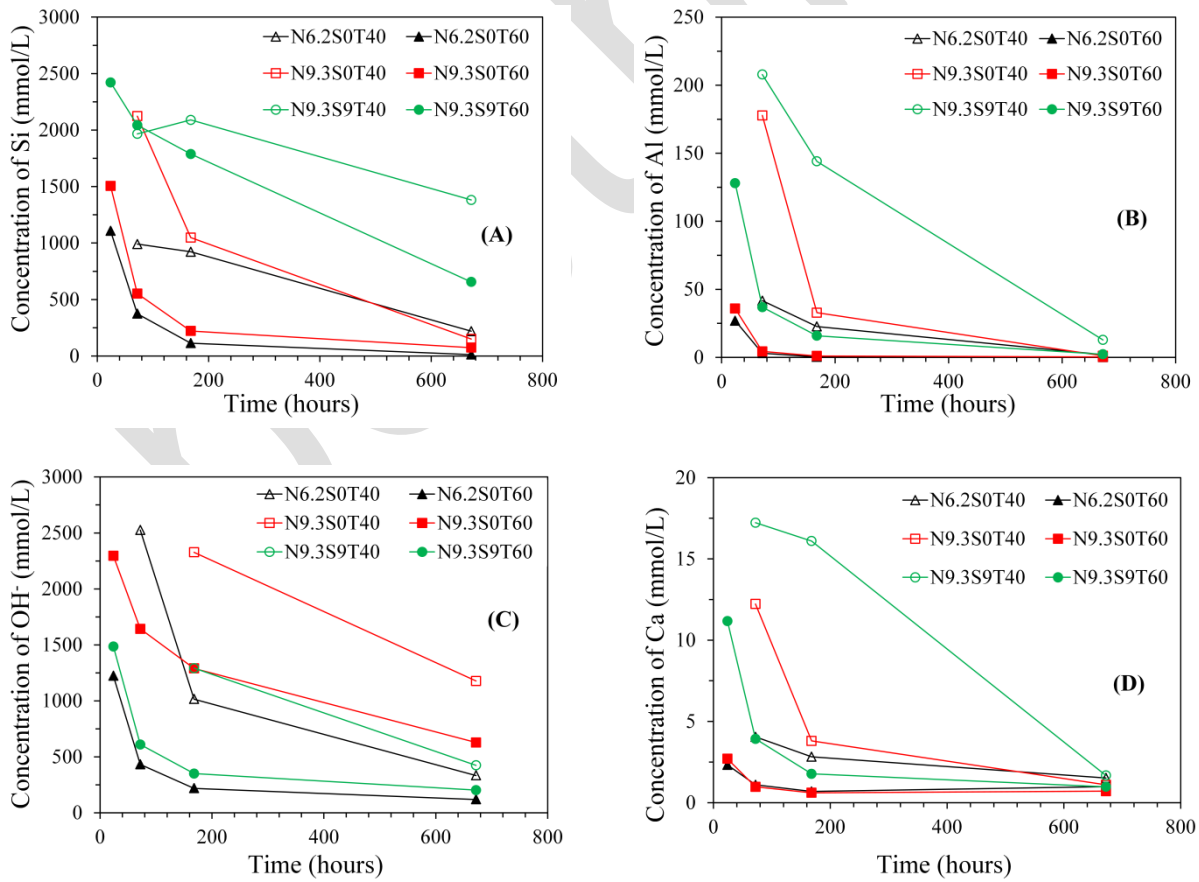


**Figure 7** Effective saturation indexes with respect to  $C_2ASH_8$ ,  $C_3AH_6$ ,  $C_4AH_{13}$  and  $Ca(OH)_2$  as functions of time. In the graphs, N and S indicate the weight percentage of  $Na_2O$  and  $SiO_2$  with respect to slag. The curing temperature was 20 °C. The water to slag ratio was 0.4. A ESI of 0 indicates equilibrium between solution and solid; a positive ESI indicates oversaturation and a negative ESI indicates undersaturation.



**Figure 8** X-ray diffraction patterns of N4S0, N8S0 and N4S5.4 at 28 days. In the graphs, N and S indicate the weight percentage of  $\text{Na}_2\text{O}$  and  $\text{SiO}_2$  with respect to slag. The curing temperature was  $20^\circ\text{C}$ . The water to slag ratio was 0.4.

1228



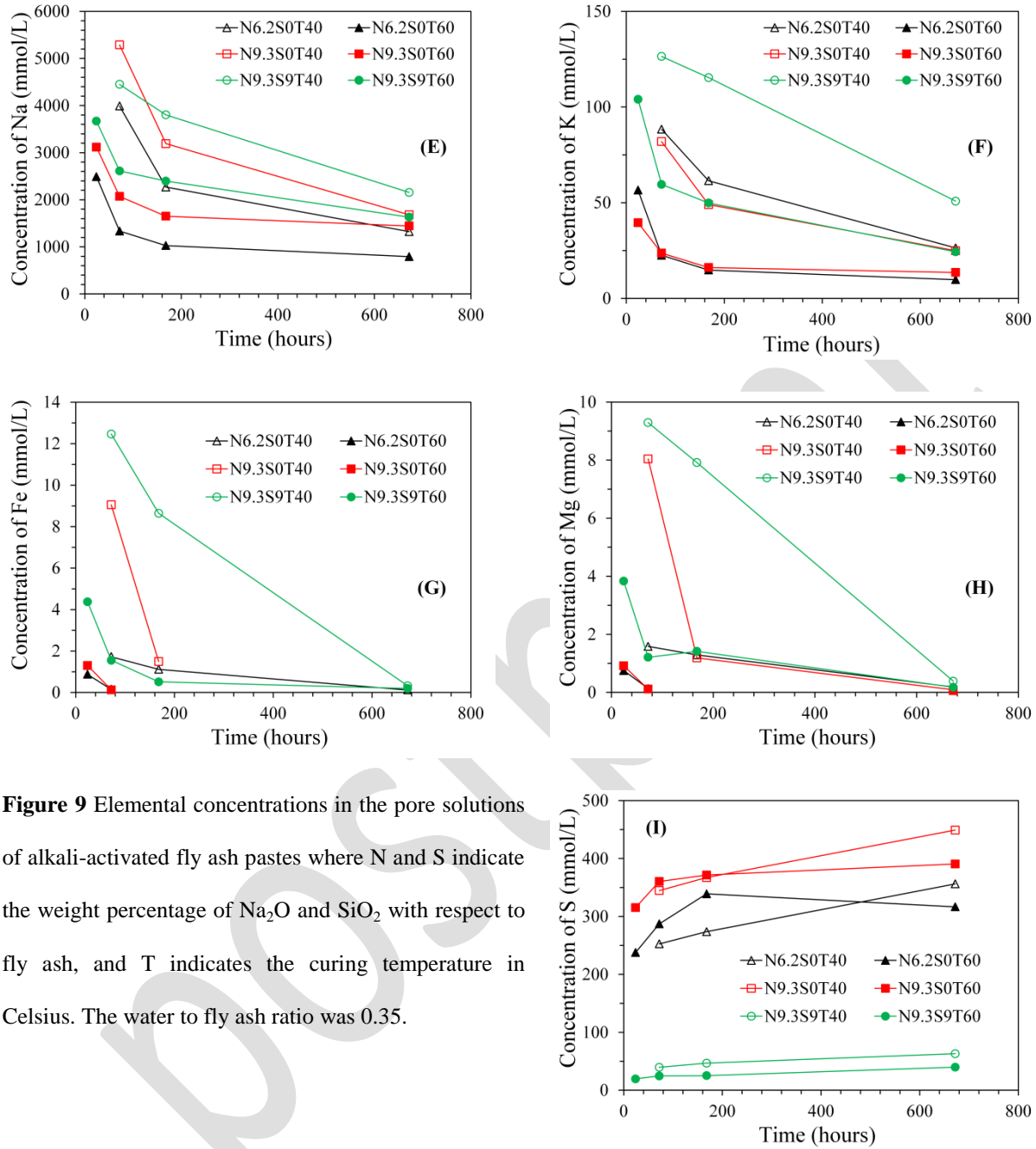


**Figure 9** Elemental concentrations in the pore solutions of alkali-activated fly ash pastes where N and S indicate the weight percentage of  $\text{Na}_2\text{O}$  and  $\text{SiO}_2$  with respect to fly ash, and T indicates the curing temperature in Celsius. The water to fly ash ratio was 0.35.

1229

1230

1231

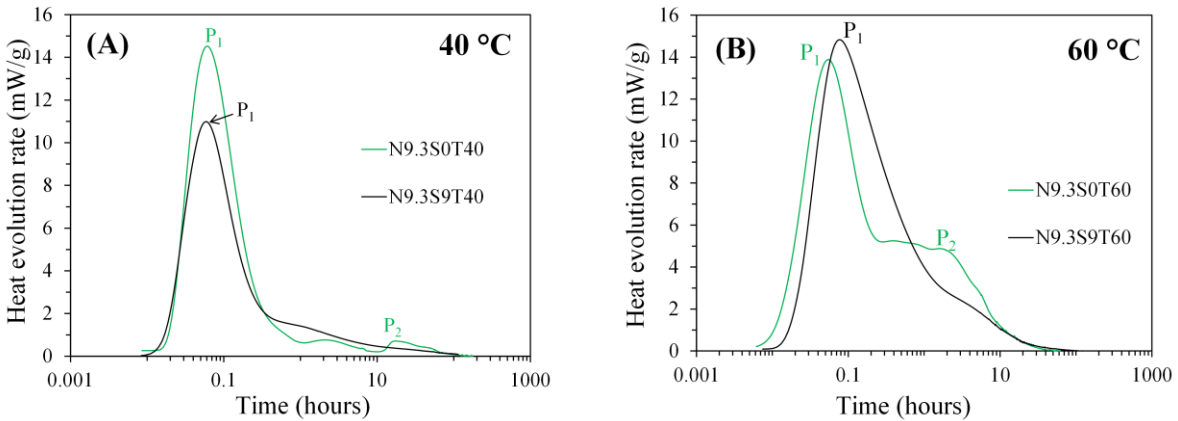


**Figure 10** Heat evolution rates of sodium hydroxide activated fly ash and sodium silicate activated fly ash cured at 40 °C and 60 °C: (A) N9.3S0T40 in comparison with N9.3S9T40; and (B) N9.3S0T60 in comparison with N9.3S9T60. In the graphs, P<sub>1</sub> and P<sub>2</sub> refer to the first and second calorimetric peak respectively, N and S indicate the weight percentage of Na<sub>2</sub>O and SiO<sub>2</sub> with respect to fly ash, and T indicates the curing temperature in Celsius. The water to fly ash ratio was 0.35.

1232

1233

1234

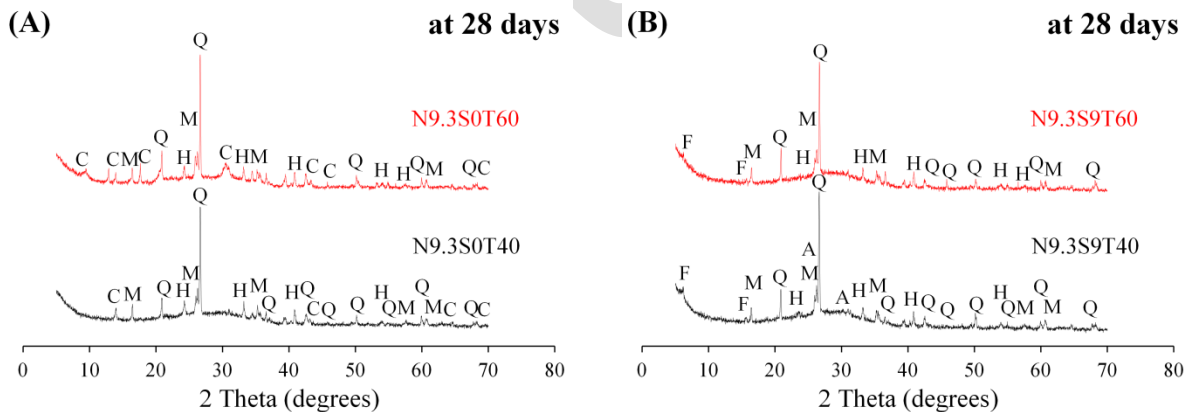


**Figure 11** X-ray diffraction patterns of alkali-activated fly ash samples cured at 40 °C and 60 °C: (A) N9.3S0T40 and N9.3S0T60; and (B) N9.3S9T40 and N9.3S9T60. In the graphs, Q, M, H, C, F and A refer to quartz, mullite, hematite, chabazite, faujasite and analcime respectively, N and S indicate the weight percentage of Na<sub>2</sub>O and SiO<sub>2</sub> with respect to fly ash, and T indicates the curing temperature in Celsius. For all samples, the water to fly ash ratio was 0.35.

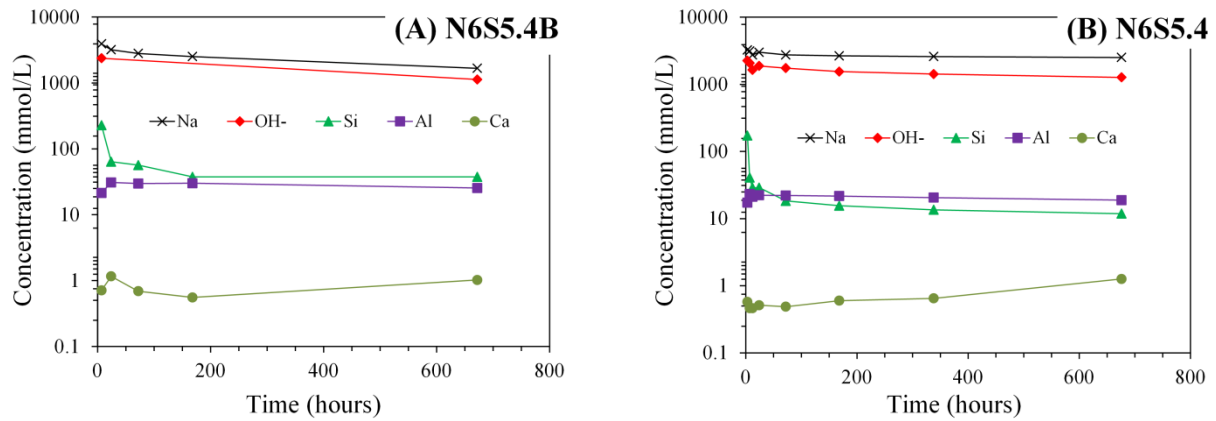


**Figure 12** Elemental concentrations in the pore solutions of alkali-activated slag blended with fly ash paste (A), and alkali-activated slag paste (B). In the graphs, N and S indicate the weight percentage of Na<sub>2</sub>O and SiO<sub>2</sub> with respect to the precursor (slag, or blend of slag and fly ash), and B indicates blend of slag and fly ash. The curing temperature was 20 °C. The water to precursor ratio was 0.4.

1235

1236

1237

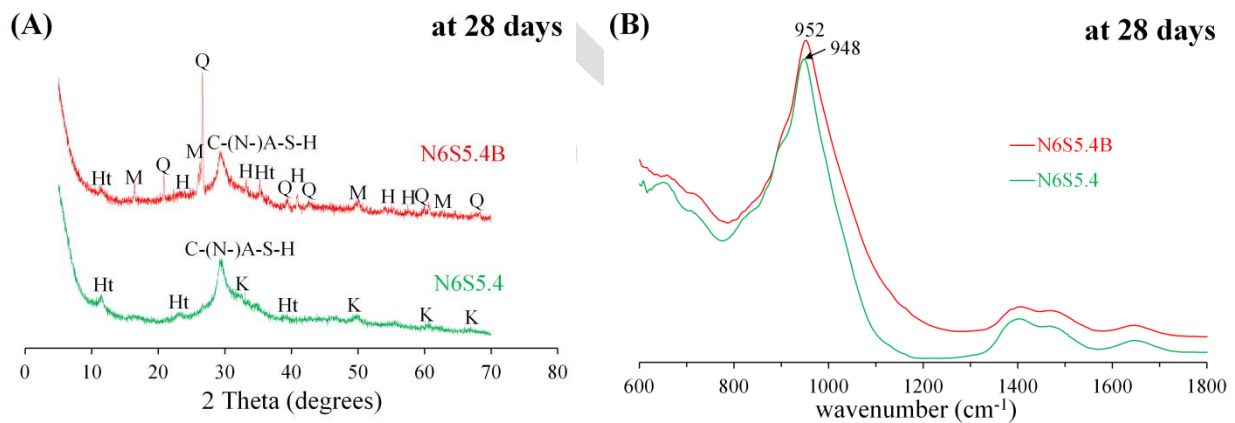


**Figure 13** Solid phase analysis of alkali-activated slag blended with fly ash and alkali-activated slag with the same alkaline activator: (A) X-ray patterns, and (B) FTIR spectra. In the graphs, Q, M, H, Ht, K and C-(N-)A-S-H refer to quartz, mullite, hematite, hydrotalcite, katoite and calcium aluminosilicate hydrate respectively, N and S indicate the weight percentage of Na<sub>2</sub>O and SiO<sub>2</sub> with respect to the precursor (slag, or blend of slag and fly ash), and B indicates blend of slag and fly ash. The curing temperature was 20 °C. The water to precursor ratio was 0.4.

1238

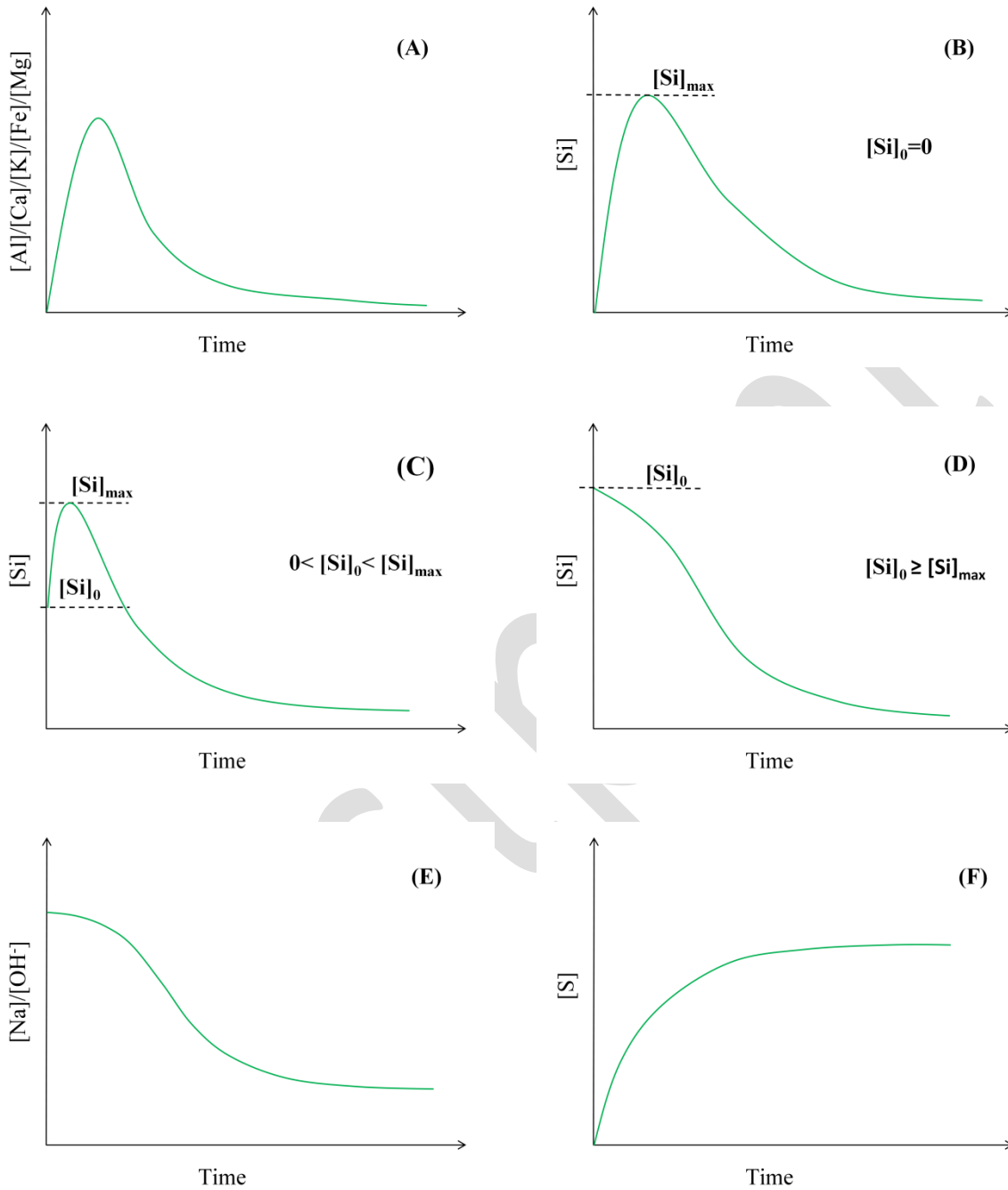


**Figure 14** Conceptual models to describe the concentrations of Al, Ca, K, Fe, Mg, Si, Na, OH<sup>-</sup> and S in the pore solution of alkali-activated slag/fly ash paste. In the graphs, [Si]<sub>0</sub> is the concentration of Si in the alkaline activator. [Si]<sub>max</sub> is the maximum concentration of Si.

1239

1240

1241

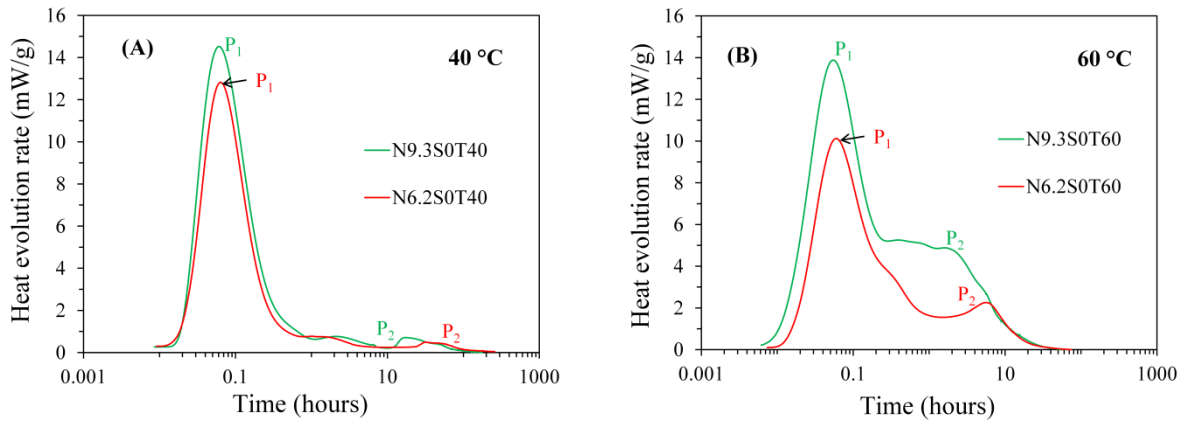


**Figure 15** Heat evolution rates of alkali-activated fly ash pastes at 40 °C (A) and 60 °C (B). In the graphs, P<sub>1</sub> and P<sub>2</sub> refer to the first and second calorimetric peak respectively, N and S indicate the weight percentage of Na<sub>2</sub>O and SiO<sub>2</sub> with respect to fly ash, and T indicates the curing temperature in Celsius. The water to fly ash ratio was 0.35.

1242

1243

1244

1245

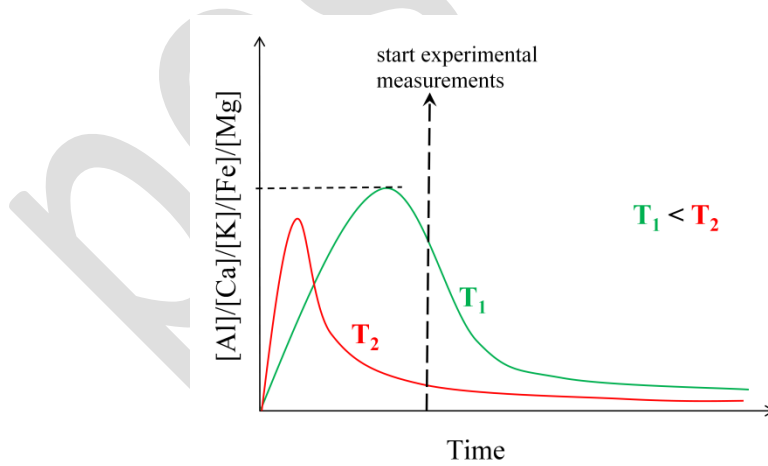


**Figure 16** The influence of an increase of temperature on the concentrations of Al, Ca, K, Fe and Mg in the pore solution of alkali-activated fly ash paste. T<sub>1</sub> and T<sub>2</sub> are temperatures.

1246

1247

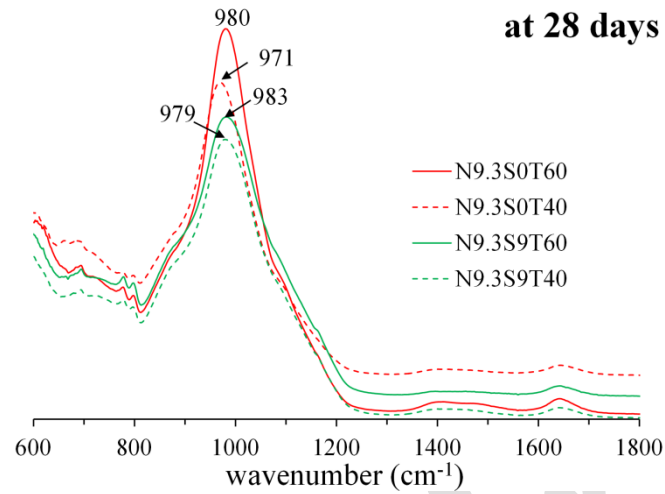


**Figure 17** FTIR spectra of alkali-activated fly ash samples at 28 days. In the graph, N and S indicate the weight percentage of Na<sub>2</sub>O and SiO<sub>2</sub> with respect to fly ash, and T indicates the curing temperature in Celsius. The water to fly ash ratio was 0.35.

1248

POSTPRINT